Science of the Total Environment 816 (2022) 151567

Contents lists available at ScienceDirect

Science of the Total Environment

journal homepage: www.elsevier.com/locate/scitotenv

Mineral characterization and composition of Fe-rich flocs from wetlands of Iceland: Implications for Fe, C and trace element export

Laurel K. ThomasArrigo [a,*], Luiza Notini [a], Jeremiah Shuster [c], Tabea Nydegger [a], Sophie Vontobel [a], Stefan Fischer [c], Andreas Kappler [b], Ruben Kretzschmar [a]

[a] Soil Chemistry Group, Institute of Biogeochemistry and Pollutant Dynamics, Department of Environmental Systems Science, ETH Zurich, Universitätstrasse 16, CHN, CH-8092 Zürich, Switzerland
[b] Geomicrobiology Group, Centre for Applied Geosciences (ZAG), University of Tübingen, Schnarrenbergstrasse 94-96, D-72076 Tübingen, Germany
[c] Tübingen Structural Microscopy Core Facility, Centre for Applied Geosciences (ZAG), University of Tübingen, Schnarrenbergstrasse 94-96, D-72076 Tübingen, Germany

HIGHLIGHTS

- Accumulations of Fe-rich flocs are common in Icelandic wetlands.
- Floc Fe minerals are dominated by poorly-crystalline ferrihydrite and lepidocrocite.
- Floc (bio)organics comprise mineral encrusted microbially-derived components.
- Highly mobile flocs may contribute to Fe, C, and trace element export from wetlands.

GRAPHICAL ABSTRACT

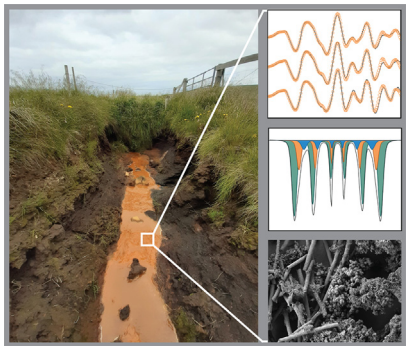

ARTICLE INFO

Article history:
Received 25 September 2021
Received in revised form 5 November 2021
Accepted 5 November 2021
Available online 8 November 2021

Editor: Filip M.G. Tack

Keywords:
Freshwater flocs
Fe(II)-oxidizing bacteria
Biominerals
Wetlands
EXAFS
^{57}Fe Mössbauer

ABSTRACT

In freshwater wetlands, redox interfaces characterized by circumneutral pH, steep gradients in O_2, and a continual supply of Fe(II) form ecological niches favorable to microaerophilic iron(II) oxidizing bacteria (FeOB) and the formation of flocs; associations of (a)biotic mineral phases, microorganisms, and (microbially-derived) organic matter. On the volcanic island of Iceland, wetlands are replenished with Fe-rich surface-, ground- and springwater. Combined with extensive drainage of lowland wetlands, which forms artificial redox gradients, accumulations of bright orange (a)biotically-derived Fe-rich flocs are common features of Icelandic wetlands. These loosely consolidated flocs are easily mobilized, and, considering the proximity of Iceland's lowland wetlands to the coast, are likely to contribute to the suspended sediment load transported to coastal waters. To date, however, little is known regarding (Fe) mineral and elemental composition of the flocs. In this study, flocs from wetlands ($n = 16$) across Iceland were analyzed using X-ray diffraction and spectroscopic techniques (X-ray absorption and ^{57}Fe Mössbauer) combined with chemical extractions and (electron) microscopy to comprehensively characterize floc mineral, elemental, and structural composition. All flocs were rich in Fe (229–414 mg/g), and floc Fe minerals comprised primarily ferrihydrite and nano-crystalline lepidocrocite, with a single floc sample containing nano-crystalline goethite. Floc mineralogy also included Fe in clay minerals and appreciable poorly-crystalline aluminosilicates, most likely allophane and/or imogolite. Microscopy images revealed that floc (bio) organics largely comprised mineral encrusted microbially-derived components (i.e. sheaths, stalks, and EPS) indicative of common FeOB *Leptothrix* spp. and *Gallionella* spp. Trace element contents in the flocs were in the low μg/g range, however nearly all trace elements were extracted with hydroxylamine hydrochloride. This finding suggests that the (a)biotic reductive dissolution of floc Fe minerals, plausibly driven by exposure to the varied

* Corresponding author.
E-mail address: laurel.thomas@usys.ethz.ch (L.K. ThomasArrigo).

https://doi.org/10.1016/j.scitotenv.2021.151567

geochemical conditions of coastal waters following floc mobilization, could lead to the release of associated trace elements. Thus, the flocs should be considered vectors for transport of Fe, organic carbon, and trace elements from Icelandic wetlands to coastal waters.

1. Introduction

Abiotic oxidation of dissolved ferrous iron (Fe(II)) occurs rapidly in oxygenated natural waters at circumneutral pH (Davison and Seed, 1983), triggering the hydrolysis of Fe(III) and the precipitation of ferrihydrite or lepidocrocite; (poorly crystalline) Fe(III) oxyhydroxides (Schwertmann and Cornell, 2000). However, at low pO_2, the kinetics of chemical oxidation of Fe(II) are significantly slower, thus enabling biologic iron(II) oxidation processes, facilitated by microaerophilic iron(II) oxidizing bacteria (FeOB), to effectively compete with abiotic Fe(II) oxidation (Druschel et al., 2008). Specifically, FeOB (e.g., *Leptothrix* spp., *Gallionella* spp., *Sideroxydans* spp.) thrive under low pO_2 conditions found at redox interfaces characterized by steep gradients in O_2 and a continual supply Fe(II) (Emerson et al., 2010). The resulting biogenic iron oxides, often termed BIOS, vary in morphology and crystallinity. Ecological niches favorable to FeOB and BIOS formation are often found in freshwater wetlands, streams, or drainage systems where oxygenated surface waters mix with anoxic, Fe(II)-bearing spring- or groundwater. In such environments, depending on the water flow conditions, (a)biotic Fe(III) (oxyhydr)oxides may accumulate as loosely consolidated flocs or as dense mats with vibrant orange to red/brown coloration.

Natural Fe(III) (oxyhydr)oxide precipitates, both abiotic and biologically-produced, tend to be associated with organic matter (Eusterhues et al., 2008). This may occur either through sorption of or coprecipitation with dissolved organic matter (Riedel et al., 2013) or through association with bacterial exudates, which both serve as nucleation sites for Fe(III) (oxyhydr)oxide precipitation and form a matrix which entraps particulate mineral phases (Chan et al., 2009; Elliott et al., 2012; Cockell et al., 2011). The presence of (microbially-derived) organic matter in flocs influences physicochemical properties of the floc Fe(III) (oxyhydr)oxides; association with organic matter induces changes in the aggregate and mineral morphology and structure and the mineral surface charge compared to a pure Fe(III) (oxyhydr)oxide (Eusterhues et al., 2008; Mikutta et al., 2008; ThomasArrigo et al., 2019; Kikuchi et al., 2019). In addition, natural organic matter supplies a heterogeneous mixture of variably charged functional groups. Collectively, these physicochemical changes influence overall floc sorption capacity. Trace element enrichments are often reported in natural flocs (Elliott et al., 2012; Plach et al., 2011; Plach et al., 2014; Plach and Warren, 2012; ThomasArrigo et al., 2014; Ferris et al., 2000; Ferris et al., 1999; Tessier et al., 1996) and in model studies, the appreciable sorption capacity of natural floc samples (or BIOS) has been demonstrated for multiple trace elements (e.g., As (Sowers et al., 2017), Cd (Martinez et al., 2004), Cr (Whitaker et al., 2018), Cs (Kikuchi et al., 2019), Cu (Whitaker and Duckworth, 2018; Field et al., 2019), I (Kennedy et al., 2011), P (Field et al., 2019; Buliauskaitė et al., 2020; Rentz et al., 2009), Pb (Whitaker and Duckworth, 2018), Se (Kikuchi et al., 2019), Sr (Langley et al., 2009), and Zn (Whitaker and Duckworth, 2018)) and dissolved organic matter (Sowers et al., 2019). Thus flocs, comprising a distinct environmental compartment separate from sediments (Plach and Warren, 2012), influence the partitioning and biogeochemical cycles of trace elements.

However, flocs are both biogeochemically and physically dynamic. Relying on the surrounding waters to supply the components (e.g., organic detritus, inorganic particulate matter, Fe(II), nutrients) necessary for floc formation and growth (Droppo, 2001), floc structural and mineral composition changes with the varying geochemical conditions of the surrounding waters (Perret et al., 2000). For example, Baken et al. (2013) demonstrated that freshly precipitated Fe-rich material formed via oxidation of Fe(II)-bearing groundwater in the Kleine Nete catchment (Belgium) comprised ferrihydrite-like mineral phases, whereas suspended sediments collected further downstream had lower Fe content and more crystalline Fe phases, indicating the ageing of precipitates and increased mixing with allochthonous material with increasing stream order. Loosely consolidated floc material may also be physically mobilized by changes in energy regimes associated to storm events (e.g., wind, waves, or rain) (Plach et al., 2011; Plach et al., 2014; Carlile and Dudeney, 2000), with implications for floc mineral composition and trace element sequestration (Plach et al., 2011; Plach et al., 2014). Floc microbial communities are also influenced by the geochemical composition of the surrounding waters (Fleming et al., 2014; McBeth et al., 2013) and are subject to seasonal shifts (Fleming et al., 2014; Gault et al., 2012; Elliott and Warren, 2014), with similar implications for floc mineral composition (Gault et al., 2012; Elliott and Warren, 2014) and trace element sequestration (Elliott and Warren, 2014).

On the volcanic island of Iceland, surface-, ground- and spring waters are replenished with a continuous supply of Fe resulting from the weathering of basalt minerals and high rates of aeolian deposition of Fe-rich basaltic volcanic glass (10 to >250 g m^{-2} yr^{-1}) (Arnalds, 2010). In combination with appreciable precipitation (>600 mm/yr across most of Iceland (Arnalds, 2015)), this Fe-rich water sustains ~9000 km^2 of inland mainly minerotrophic wetlands, which account for 19% of Iceland's vegetated land surface (Arnalds et al., 2016). Owing to this abundance of Fe, accumulations of (a)biotically-derived Fe-rich flocs are common features of Icelandic wetlands (Cockell et al., 2011; Arnalds, 2015; Arnalds et al., 2016). Additionally, ~47% of Icelandic wetlands are impacted by drainage (Arnalds et al., 2016). Nearly 30,000 km of ditches connect wetland drainage networks to streams and rivers (Arnalds et al., 2016) and simultaneously form artificial redox gradients which facilitate (a)biotic Fe(II) oxidation and floc accumulation. With the vast majority of impacted wetlands found below 200 m elevation (Arnalds et al., 2016), the proximity of low elevation wetlands and drainage networks to the coast, combined with occasionally intense rainfall events (>100 mm/day) (Arnalds, 2015; Olafsson et al., 2007) which can easily wash out the highly mobile flocs (Fig. S1), suggest that mobilized Fe-rich flocs are likely to contribute to the suspended sediment load transported to coastal waters.

Previously, Cockell et al. (2011) sampled bright orange precipitates collected from microbial mats found in two cold (MAT <5 °C) Icelandic streams. Their research focused on the composition of microbial communities inhabiting the mats; utilizing 16S rRNA gene sequencing and (electron) microscopy techniques, Cockell et al. (2011) identified both FeOB (*Leptothrix* spp., *Gallionella* spp.) and iron reducing bacteria (FeRB; *Geobacter* spp.). Analyses of floc (Fe) mineral composition was limited; a qualitative assessment with X-ray diffraction (XRD) and Raman microscopy identified amorphous and crystalline Fe phases, feldspars and pyroxenes (Cockell et al., 2011). Therefore, in this study, Fe-rich flocs from shallow surface streams, cold seeps, and peat soil seepages across western Iceland ($n = 16$) were collected for comprehensive mineral, elemental, and structural characterization. Floc (Fe) mineralogy was investigated using a combination of XRD, ^{57}Fe Mössbauer spectroscopy, and Fe *K*-edge X-ray absorption spectroscopy (XAS) including shell-fit and Wavelet Transform analyses. Solid-phase chemical extractions were used to confirm Fe mineralogy, and, in combination with elemental analyses of the flocs and surrounding surface waters, enabled an assessment of the long-term sequestration potential of flocs for trace elements and organic carbon. Because of the high probability of floc mobilization and transport (Fig. S1), characterization of floc (Fe)

mineralogy and floc structural and biogeochemical composition is critical to understanding factors influencing the cycling, export, and fate of Fe, trace elements, and organic carbon in Fe-rich Icelandic wetlands.

2. Materials and methods

2.1. Study sites, floc sampling and characterization

Loosely-consolidated, bright orange flocs were sampled in July and August 2020 from surface streams ($n = 3$), peat soil seepages ($n = 11$), and cold seeps ($n = 2$) situated in (un)disturbed wetlands located across south, south-west, west, and north-west Iceland (Figs. 1 and S2, Table S1). All sampled flocs were submerged at the time of sampling. Depending on the thickness of the floc layer (~2 to >20 cm), the flocs were collected either in 20 mL glass vials (Fig. 1A) or in 500 mL beakers, where they rapidly settled (<2 min), enabling decanting of the surrounding water. For the sites with thin floc layers (~2 cm), multiple floc samples were collected within a 2 m^2 area to ensure sufficient solid-phase material for analyses. The decanted flocs were transported on ice and within 3 h were spread thinly on ceramic plates and air-dried in an oven at 30 °C overnight. Dried floc material was then sieved (<200 μm), gently homogenized with a mortar and pestle, and stored in brown glass in a desiccator.

At each site, surface water directly above the flocs was analyzed on-site for pH using indicator strips (MColorpHast™, pH 4–7) or Special indicator (pH 6.4–8, Merck), temperature and electrical conductivity (WTW 315i), and redox potential (custom probe; a fiberglass shell equipped with partially embedded Pt sensors and connected through cables to a Ag/AgCl saturated KCl reference electrode, PaleoTerra, NL). In addition, surface water samples were collected using Rhizon CSS samplers with a <0.15-μm cut-off and PE/PVC tubing (Rhizosphere Research Products) connected to a pre-acidified syringe (HCl, Normatron®, VWR). Aliquots of the acidified surface water samples (pH <4) were crimp-sealed in 20-mL glass vials and transported and stored in the

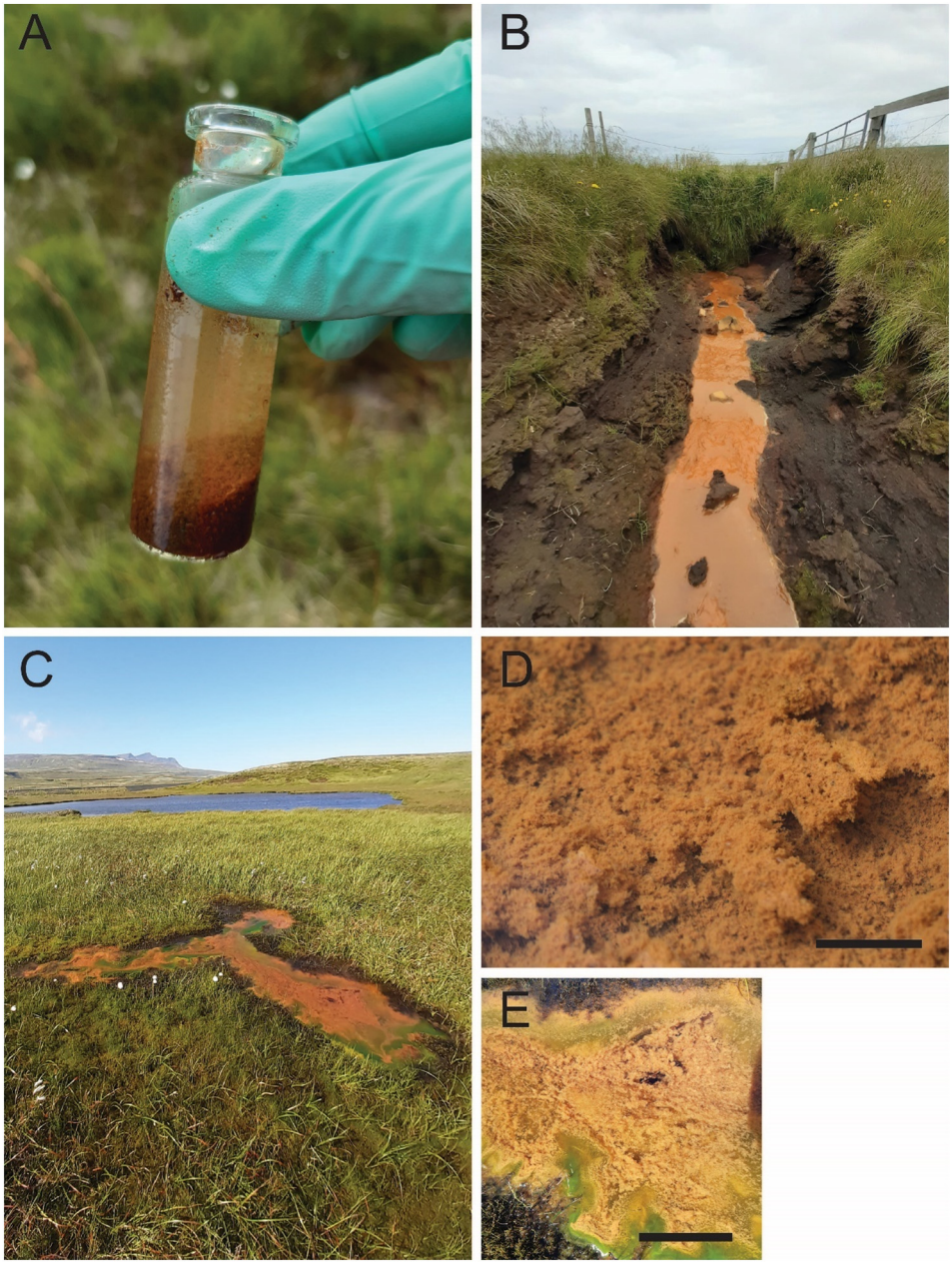

Fig. 1. Examples of iron-rich floc precipitates. (A) Settled flocs during sampling. (B) Typical peat soil seepage (site F10). (C) Iron-rich cold spring (site F9). (D) and (E) are detailed pictures of drainage ditch flocs (D) and cold spring flocs (E). Scale bars in (D) and (E) are 2 cm and 10 cm, respectively.

dark at 4 °C prior to analysis for dissolved organic carbon and nitrogen (pH < 4; DIMA-N coupled to a Dimatoc 2000 TOC analyzer, Dimatec). To account for potential contamination of the samples by the syringe, additional blanks ($n = 5$) with doubly deionized (DDI) water (Milli-Q®, Millipore, 18.2 MΩ·cm) were prepared in the laboratory following the same sampling procedure as employed in the field. The remaining acidified surface water samples (pH <4) were further acidified in the field (pH <1), and were similarly crimp-sealed in 20-mL glass vials and transported and stored in the dark at 4 °C prior to analysis for total element content analyses (inductively coupled plasma-optical emission spectrometry, ICP-OES, Agilent 5100; inductively coupled plasma-mass spectrometry, ICP-MS, Agilent 8800 Triple Quad). For these analyses, additional blanks ($n = 5$) of acidified DDI water were prepared in the field, handled following the same procedure as the surface water samples, and measured to account for potential Si leaching from the glass vials during sample transport and storage. Dissolved Fe speciation in the surface water (Fe(total) and Fe(II)) was also measured with the 1,10-phenanthroline method (Loeppert and Inskeep, 1996), whereby Fe(II) was determined after an excess of nitriloacetic acid was added to mask the Fe(III) (Mikutta, 2011).

Major and trace element contents of the flocs were determined with ICP-OES and ICP-MS following microwave-assisted acid digestion (0.6:1 H_2O_2:HNO_3, MLS turboWave). Due to the presence of white precipitates in the digests, it possible that the microwave digestion did not completely dissolve crystalline aluminosilicates present in the floc matrix. An additional hydroxylamine hydrochloride extraction (Lovley and Phillips, 1987) was therefore used to estimate the amount of trace metal (loid)s associated to poorly-crystalline aluminosilicates (e.g., allophane and imogolite) and iron phases (e.g., ferrihydrite, poorly-crystalline lepidocrocite) (Dahlgren, 1994). For these analyses, 20 mg of dried floc material was added to 5 mL of 0.25 M hydroxylamine hydrochloride in 0.25 M HCl in 50-mL centrifuge tubes. After vortex mixing (10 s), samples were placed in a 50 °C oven for 1 h, during which time they were occasionally shaken. Prior to analysis with ICP-OES and ICP-MS, digests and extracts were filtered (0.45 μm, nylon) to remove residual solids. Total C and N contents of the flocs were determined with an elemental analyzer (CHNS-932, LECO, $n = 2$). Attenuated total reflectance Fourier-transform infrared (ATR-FTIR) spectroscopy was used to characterize functional groups of the (in)organic fractions in the flocs. The spectra were recorded with a resolution of 4 cm^{-1} on a Frontier FT-IR Spectrometer (Perkin Elmer) with a universal attenuated total reflectance (UATR) three-reflection diamond/ZnSe crystal and MIRTGS detector. Thirty-six scans per sample were co-added and background corrected using the Perkin Elmer Frontier IR software program.

2.2. Microscopy imaging

At selected sites, additional decanted floc material was collected and stored in glass vials at 4 °C in the dark for microscopy imaging. For light microscopy imaging, fresh floc material was pipetted onto glass slides, covered and dried at room temperature, and imaged with a Zeiss Axioskop 40. For scanning electron microscopy (SEM) analysis, 25% electron microscopy-grade glutaraldehyde (0.2 mL) was added to each sample (1.8 mL) for an overall 2.5% glutaraldehyde concentration to fix any cells that may be present. The samples were incubated at 4 °C in the dark for 24 hs. After incubation, DDI water was added to the fixed samples to dilute the floc concentration (4 mL final volume). Note that cover glass slides were prepared in advance. Briefly, glass slides were coated with 50 μL 0.1% Poly-L-Lysine solution (PLANO, Wetzlar, item number 18026) and dried at 60 °C in an incubator for 1 h. Using a 24-well plate, the prepared glass slides were placed at the bottom of the wells. Aliquots of the diluted samples were transferred to separate wells each containing a Poly-L-Lysine coated glass slide. The plate was covered with a lid and incubated at room temperature for 30 min allowing the flocs to settle onto the coated slides. From each well, the supernatant was removed and DDI water was added to wash the sample (10 min incubation); this washing procedure was repeated by removing the supernatant and adding "fresh" DDI water. After washing, the samples were dehydrated using a graded ethanol series (30, 70, and 95% for 5 min each concentration; 2 × 100% for 30 min). In the final step, the sample-bearing slides were dipped into a FIA vial containing 1:1 hexamethyldisilazane (HMDS):100% ethanol for 30 s. The sample was subsequently dipped into a second vial containing 100% HMDS for 30 s. All samples were allowed to air dry on filter paper. The sample-bearing glass slides were attached to aluminium stubs using carbon adhesive tabs (PLANO, Wetzlar, item numbers G301 & G3347) and coated with ~8 nm of Pt using a BAL-TEC SCD 005 sputter coater. The structural and chemical characterization of the flocs was performed using a Crossbeam 550L Focused Ion Beam (FIB) – Scanning Electron Microscope (Zeiss, Oberkochen, Germany) operating at an acceleration voltage of 1 kV and working distances of 4 mm. All micrographs were taken using the Secondary Electron Secondary Ion (SESI) detector.

2.3. X-ray diffraction

Quantitative mineral-phase analyses were performed by powder X-ray diffraction (XRD, D8 Advance, Bruker) with Rietveld analysis. Dried sample material (~5 mg) was resuspended in ethanol (~30 μL, Merck) and pipetted onto a polished silicon wafer (Sil'tronix Silicon Technologies, France). Samples were analyzed in Bragg−Brentano geometry using Cu Kα radiation (λ = 1.5418 Å, 40 kV, and 40 mA) and a high-resolution energy-dispersive 1-D detector (LYNXEYE). Diffractograms were recorded from 10° to 70°2θ with a step size of 0.02°2θ and 10 s acquisition time per step. The relative contributions of mineral phases in diffraction patterns were determined by Rietveld Quantitative Phase Analysis (QPA) using the TOPAS software (Version 5, Bruker AXS) in combination with published crystallographic structure files with 2-line ferrihydrite included as mass-calibrated PONKCS (Partial Or No Known Crystal Structure) (Scarlett and Madsen, 2006) phase. The validity of this method has been previously tested and published (ThomasArrigo et al., 2018).

2.4. Iron K-edge X-ray absorption spectroscopy

Iron oxidation state and speciation in select floc samples was analyzed by bulk Fe *K*-edge (7112 eV) X-ray absorption spectroscopy (XAS) at the SAMBA beamline of SOLEIL (Saint-Aubin, France). For these measurements, dried floc material was pressed into 10-mm pellets and sealed with Kapton® tape. Transmission Fe X-ray absorption near edge structure (XANES) and extended X-ray absorption fine structure (EXAFS) spectra were recorded in continuous scan mode at ~80 K using a N_2(1) cryostat and a Si(220) monochromator calibrated to the first-derivative maximum of the *K*-edge absorption spectrum of a metallic Fe foil (7112 eV). The foil was continuously monitored to account for small energy shifts (<1 eV) during the sample measurements. Higher harmonics in the incoming beam were eliminated by mirrors. Four to ten scans were collected and averaged. All spectra were energy calibrated, pre-edge subtracted, and post-edge normalized in Athena (Ravel and Newville, 2005) with the edge-energy, E_0, defined as zero-crossing in the second XANES derivative. Linear combination fit (LCF) analyses of k^3-weighted Fe *K*-edge XANES spectra were conducted over an energy range of −20 to 30 eV (E - E_0) with E_0 of sample and reference compound spectra defined as zero-crossing in their second XANES derivative. Linear combination fit analyses of k^3-weighted Fe *K*-edge EXAFS spectra were performed over a k-range of 2–12 $Å^{-1}$ with the E_0 of all spectra and reference compounds set to 7128 eV. No constraints were imposed during LCF analyses, and initial fit fractions were recalculated to a compound sum of 100%. Iron reference compounds for LCF analysis were selected after principal component analysis and target-transform testing (see Supporting Information, Section 6).

Fourier transforms of k^3-weighted EXAFS spectra were calculated over a k-range of 2–12 $Å^{-1}$ using a Kaiser-Bessel window function with a sill width of 3 $Å^{-1}$. The frequency cut-off parameter, Rbkg, was set to 1.0. Shell-fit analyses of k^3-weighted EXAFS spectra were performed in R-space (R-range = 1.0–3.5 Å, k-range 2–12 $Å^{-1}$) with Artemis (Ravel and Newville, 2005). Theoretical phase-shift and amplitude functions were calculated with FEFF v.6 (Zabinsky et al., 1995) based on the structures of goethite (Kaur et al., 2009) (α-FeOOH) and lepidocrocite (Zhukhlistov, 2001) (γ-FeOOH). To qualitatively assess contributions from low Z backscattering atoms in the second coordination shell of the floc samples, we also conducted Morlet wavelet transform (WT) analyses on k^2-weighted Fe K-edge EXAFS spectra using the Fortran-based HAMA code (Funke et al., 2005). Overview ($R + \Delta R$-range = 0.5–4 Å; $\kappa = 8$, $\sigma = 0.8$) and high resolution ($R + \Delta R$-range = 2.3–3.5 Å; $\kappa = 4$, $\sigma = 2$) WTs of floc samples were compared to the reference compounds used in LCF analyses.

2.5. ^{57}Iron Mössbauer spectroscopy

Selected floc samples were additionally analyzed with ^{57}Fe Mössbauer spectroscopy. Mössbauer spectra were obtained using a ^{57}Co/Rh γ-radiation source with an activity of ~50 mCi vibrated in a constant acceleration mode in a standard setup (WissEl, Wissenschaftliche Elektronik GmbH). Sample material (60–80 mg) was sealed between two layers of Kapton® tape within a plastic circular frame (10 mm). All samples were mounted in transmission geometry. Sample temperatures were maintained with a closed-cycle cryostat (SHI-850-5, Janis Research Co.), whereas the ^{57}Co/Rh source remained at room temperature. Spectra were collected at 77 K and 4.2 K and analyzed using the Recoil software (University of Ottawa, Canada) by applying an extended Voigt-based fitting routine (Lagarec and Rancourt, 1997). The spectra were calibrated against 7 μm thick α-^{57}Fe(0) at 295 K, and center shifts (CS) are quoted relative to this. For all samples, the half width at half-maximum was fixed to 0.135 mm s^{-1}; the value of the inner line broadening of the calibration foil at 295 K.

3. Results and discussion

3.1. Surface water geochemistry

In surface waters directly above the flocs, temperatures ranged from 3.9 to 13.4 °C ($\bar{x}$ = 10.1), with the lowest temperatures recorded in surface waters of cold seeps (F6 and F9, 3.9 °C). The pH was relatively similar at all sites (6.1–6.7, $\bar{x}$ = 6.4), redox potential ranged from +215 to +421 mV ($\bar{x}$ = 335), and electrical conductivity values varied between 62 and 479 μS/cm ($\bar{x}$ = 191). This information is presented in Table S1. Total element concentrations of surface water samples are shown in Table S2. Measured DOC concentrations ranged from 4.71 to 27.14 mg/L ($\bar{x}$ = 10.68). Dissolved concentrations of cations were generally higher than concentrations previously reported for non-geothermal natural waters in Iceland (e.g., ground waters, lakes, and rivers). However, they were in good agreement with previously reported dissolved element concentrations in Icelandic peat surface waters and peat soil seepages (Stefánsson et al., 2005; Stefánsson et al., 2001; Arnórsson et al., 2002). Dissolved concentrations of Al (0.26–4.63 mg/L, $\bar{x}$ = 1.23) and Si (6.57–19.64 mg/L, $\bar{x}$ = 12.17) in Icelandic surface waters are thought to derive solely from weathering of basaltic rocks, and concentrations often near saturation for the precipitation of the poorly crystalline aluminosilicate minerals (e.g., Al-rich allophane) (Stefánsson and Gíslason, 2001). Trends in concentrations of dissolved cations also followed the order Na > Ca > Mg > K (Na; 5.60–41.41 mg/L, $\bar{x}$ = 15.16, Ca; 4.00–33.37 mg/L, $\bar{x}$ = 11.32, Mg; 1.48–17.98 mg/L, $\bar{x}$ = 8.15, K; 0.20–2.11 mg/L, $\bar{x}$ = 0.81), in agreement with previous surface water samples collected from Icelandic streams largely influenced by weathering of basaltic materials (Stefánsson and Gíslason, 2001). Concentrations of dissolved Fe were generally low at most sites (<2 mg/L), with exceptions at F6, F10, F13, and F16, where dissolved Fe concentrations were 22.84, 11.64, 3.36, and 6.57 mg/L, respectively. At each site, Fe(II) contributed significantly to the total dissolved Fe measured (50–97%, $\bar{x}$ = 73). Significant contributions of Fe(II) to the total concentrations of dissolved Fe in pH circumneutral, non-geothermal natural waters has previously been reported for Icelandic streams and peat surface waters (Stefánsson et al., 2005; Stefánsson et al., 2001) and likely reflect the continuous supply of Fe resulting from weathering and dissolution of Fe-rich basalt rocks (Stefánsson et al., 2005; Stefánsson and Gíslason, 2001). Considering the calculated Fe(III):DOC molar ratios (0.001–0.035, Table S2) and geochemical parameters measured at each site (e.g., pH, Table S1) it is most likely that the dissolved Fe(III) was organically complexed.

3.2. Floc characterization and major element contents

Light microscopy and SEM imaging revealed significant diversity in floc composition (Fig. 2, Fig. S3). Hollow tubes (partially) encrusted with disordered iron minerals are clearly visible in floc samples F5, F9, F12, resembling sheaths formed by the microaerophilic Fe(II)-oxidizing *Leptothrix* spp. (Chan et al., 2009; Fleming et al., 2014) *Leptothrix*-type sheaths are, to a lesser extent, also visible in floc sample F10, while very few examples of sheaths or twisted stalks characteristic of the microaerophilic Fe(II)-oxidizers *Gallionella* spp. were identified in flocs from site F6 (Fig. S3). In general, *Leptothrix*-type sheaths were more abundant than *Gallionella*-type twisted stalks, although both have been identified previously in Icelandic microbial mat samples (Cockell et al., 2011). Fleming et al. (Fleming et al., 2014) reported a similar dominance of *Leptothrix* spp. in microbial mat samples from a stream in Boothbay Harbor, Maine (USA) during the summer months, suggesting that *Leptothrix* spp. thrived in the presence high concentrations of dissolved Fe, Mn, and DOC. In contrast, *Gallionella* spp. was found to dominate the microbial mats in the early spring, associated to lower DOC concentrations (Fleming et al., 2014). Thus, considering the geochemical parameters of the surrounding surface waters (Tables S1 and S2), the abundance of *Leptothrix* spp. seems reasonable. Additional SEM images, shown in Fig. 2, highlight the diversity in floc structure and precipitate morphology. For example, in flocs from site F10, shown in Fig. 2A and B, a ribbon-like *Gallionella* stalk, (mineral encrusted) *Leptothrix*-type sheaths, aggregation of rounded μm-sized mineral precipitates as well as precipitates associated to organic and EPS structures are present. Fig. 2C (floc sample F6) shows the aggregation of smaller mineral precipitates (<300 nm) in the absence of EPS structures, and in Fig. 2D (floc sample F5), nm-sized primary precipitates are seen covering the surfaces of both mineral aggregates and organic materials. Images also revealed varied estimated inner diameters of *Leptothrix*-type sheaths within the same floc (e.g., 342 vs. 995 nm, Fig. S4D) and distinct variations in the helical structure of *Gallionella* stalks (Fig. S5).

The flocs contained 0.2–1.4 mg/g S ($\bar{x}$ = 0.8), 2.2–7.4 mg/g P ($\bar{x}$ = 3.9), and up to 153.9 mg/g C ($\bar{x}$ = 71). The lowest bulk C content was recorded for flocs from site F6 (16.5 mg/g, Table S3). Combined with the limited appearance of microbially-derived components (i.e., sheaths, stalks, and EPS) in microscopy images of flocs from site F6 (Fig. S3, Fig. 2C), these results suggest a stronger abiotic origin of iron precipitates in this floc sample and further suggest that microbially-derived organic substances, rather than peat-derived organic matter, may comprise a significant fraction of the bulk C content in the other floc samples. The composition of the organic fraction was further investigated with ATR-FTIR spectroscopy, shown in Fig. S6. Over the range of 1800–650 cm^{-1}, all flocs were similarly dominated by three major regions; two peaks at ~1636 and ~1564 cm^{-1} corresponding to C═O, C—N and N—H vibrations in amide I and II (Parikh and Chorover, 2006; Elzinga et al., 2012), a peak at ~1392 cm^{-1} relating to C═C or asymmetric C—O stretching in carboxylates (Artz et al., 2008), and variably intense peaks in the range ~1250–800 cm^{-1}, where overlapping vibrations from carbohydrates in polysaccharides (C—O, C—O—C,

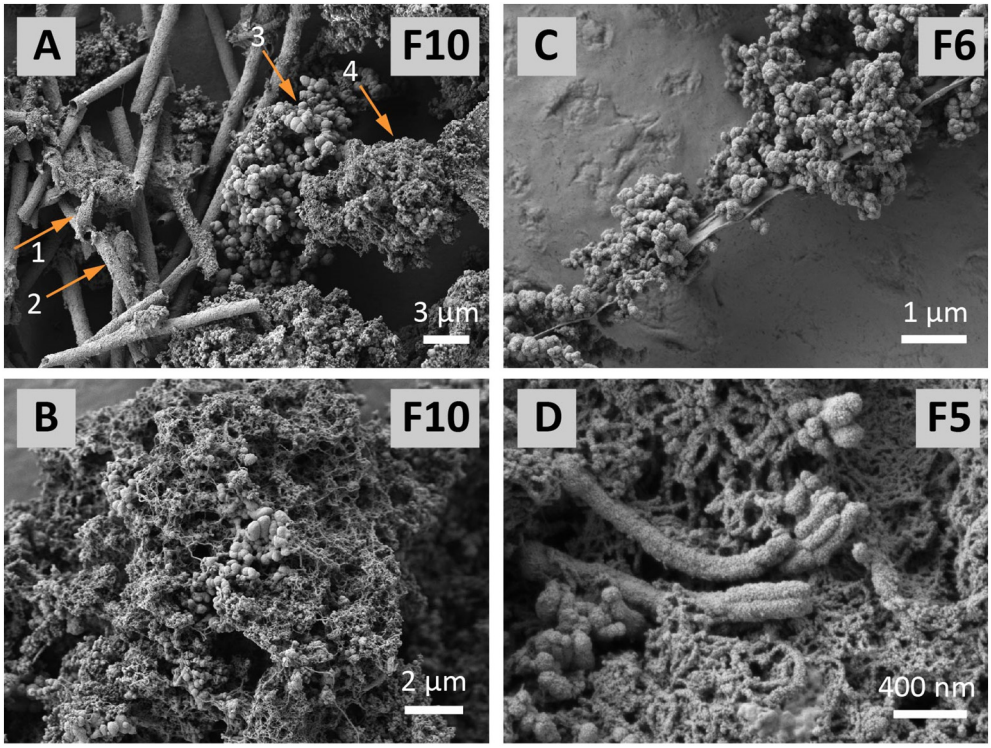

Fig. 2. Scanning electron images of floc samples. (A) Floc sample F10. Arrows point to (1) ribbon-like stalks resembling structures produced by *Gallionella* spp., (2) encrusted *Leptothrix*-type sheaths, (3) rounded mineral precipitates, and (4) precipitates associated with organic materials. (B) Floc sample F10. (C) Floc sample F6. (D) Nanometer-sized surface precipitates in floc sample F5.

C—C) (Elzinga et al., 2012), phosphorus groups (P═O, P—OH, P—OFe) (Elzinga et al., 2012), aluminosilicates (Si—O—Al) (Bishop et al., 2013), or Si-adsorbed ferrihydrite (Si—O—Fe) (Swedlund et al., 2009; Carlson and Schwertmann, 1981) make individual peak identification difficult. A detailed list of peak assignments is presented in Table S7.

Total element contents of the flocs, determined after microwave-assisted acid digestion, are presented in Table S3. As expected from their bright orange color (Fig. 1), the flocs were strongly enriched in Fe (229–414 mg/g, $\bar{x} = 326$). In addition, the flocs contained appreciable amounts of Al (2.0–14.0 mg/g, $\bar{x} = 6.9$) and Si (1.2–9.2 mg/g, $\bar{x} = 3.3$), although the presence of remaining white particles in the digests (probably Si-Al-containing precipitates) suggests that Al and Si contents were likely underestimated. We also performed an hydroxylamine hydrochloride extraction (Lovley and Phillips, 1987), which, in addition to ferrihydrite and poorly-crystalline lepidocrocite, efficiently extracts amorphous aluminosilicates (e.g., allophane, imogolite) (Dahlgren, 1994). Results from the hydroxylamine hydrochloride extraction are presented in Table S4. Excluding floc sample F1, Fe contents in the hydroxylamine hydrochloride extraction ranged from 252 to 493 mg/g ($\bar{x} = 380$); in good agreement with the Fe contents determined after the microwave-assisted acid digestion (Table S5). In contrast, for floc sample F1, only 133 mg/g Fe (~53% of microwave-assisted acid digested Fe) was extracted by hydroxylamine hydrochloride, suggesting the presence of more crystalline Fe mineral phases in this sample.

3.3. Flocs as scavengers of trace elements

Weathering of basaltic parent materials releases trace elements to soil solutions. However, trace element mobility may be limited in Icelandic volcanic soils due to their generally high cation exchange capacity (Arnalds, 2015; Arnalds et al., 1995). Consistent with the low concentrations of dissolved trace elements in surface waters at floc sampling sites (Table S2), trace element concentrations in the flocs, determined after microwave-assisted acid digestion, were generally in the low µg/g range (Table S3). However, distribution coefficients (K_d), calculated as the ratio between floc and dissolved trace element concentrations ($K_d = [TE]_{Floc}/[TE]_{0.15\text{-µm SW filtrate}}$), showed that Iceland flocs were enriched in all trace elements compared to surrounding surface waters (Table S6). Calculated values were consistently high ($\log K_d = 10^5$–10^6) for V, with moderate enrichments (10^3–10^4) recorded for As, Co, Cu, Mn, Ni, Pb, and Zn (Table S6).

Similar enrichments in trace element contents have been reported in other natural flocs when compared to both surrounding surface waters or to bed sediments (Elliott et al., 2012; Plach et al., 2011; Plach et al., 2014; Plach and Warren, 2012; ThomasArrigo et al., 2014; Ferris et al., 2000; Ferris et al., 1999; Tessier et al., 1996), and in laboratory model studies, the sorption capacity of natural floc samples has been demonstrated for multiple trace elements (Kikuchi et al., 2019; Sowers et al., 2017; Martinez et al., 2004; Whitaker et al., 2018; Whitaker and Duckworth, 2018; Field et al., 2019; Kennedy et al., 2011; Buliauskaitė et al., 2020; Rentz et al., 2009; Langley et al., 2009). Uptake of trace elements may be facilitated by multiple floc components. For example, floc (bio)organics, including living cells, EPS, and organic detritus, supply a variety of charged functional groups that may facilitate trace element sorption over large pH ranges (Kennedy et al., 2011; Takahashi et al., 2005; Leppard et al., 2003; Hao et al., 2016). Additionally, floc (bio)organics serve a structural role; entrapping precipitated nanoparticulate inorganic phases in matrices of EPS and acting as nucleation sites which template the growth of nanocrystalline Fe(III) (oxyhydr)oxides (Chan et al., 2009; Elliott et al., 2012; Cockell et al., 2011; Plach et al., 2011; Plach and Warren, 2012; ThomasArrigo et al., 2014; Chan et al., 2004; Fortin and Langley, 2005). Adsorption of or coprecipitation with organic matter alters the physicochemical properties of Fe(III) (oxyhydr)oxides, including influencing aggregate and mineral morphology and structure (Eusterhues et al., 2008; Mikutta et al., 2008; ThomasArrigo et al., 2019) and lowering point of zero charge (pH_{PZC}) (Mikutta et al., 2008; ThomasArrigo et al., 2019). Lower pH_{PZC} has been cited to explain increased trace element sorption capacity in organic-rich BIOS compared to pure Fe(III) (oxyhydr)oxides (Kikuchi et al., 2019; Whitaker and Duckworth, 2018), whereby sorption of

divalent cations to BIOS is promoted at circumneutral pH (Kikuchi et al., 2019; Whitaker and Duckworth, 2018; Kennedy et al., 2011). Thus, adsorption of dissolved trace elements to entrapped floc (iron) mineral phases or co-precipitation during the templated growth of Fe(III) (oxyhydr)oxides represent additional pathways through which floc (bio)organics may indirectly facilitate trace element uptake. This structural role of floc (bio)organics has been cited to explain natural trace element enrichments in organic-rich flocs (100–450 mg/g C) collected from freshwater streams and lakes in Ontario, Canada, where bulk floc C content was positively correlated to floc trace element contents or $\log(K_d)$, yet sequential extractions confirmed that poorly crystalline floc Fe minerals were primarily responsible for TE uptake (Elliott et al., 2012; Plach et al., 2011). Iceland flocs show a similar tendency, whereby the high fraction of trace elements removed during the acid hydroxylamine extraction ($\bar{x} = 82\%$, Table S5) indicates that floc trace elements may be primarily associated to poorly crystalline minerals which, based on $[TE]_{Floc}$ contents (Table S3), comprises a significant fraction of floc-Fe.

3.4. Floc mineralogy: X-ray diffraction

Quantitative interpretation of XRD patterns of natural samples comprising multiple amorphous phases is complex, if not impossible. Therefore, based on the abundance of ferrihydrite in Icelandic soils (Arnalds, 2015), the high fraction of hydroxylamine hydrochloride extractable Fe (Table S5), common reports of dominant ferrihydrite-like phases in similar BIOS or flocs (Cockell et al., 2011; Ferris et al., 2000; Ferris et al., 1999; Sowers et al., 2017; Whitaker and Duckworth, 2018; Field et al., 2019; Kennedy et al., 2011; Langley et al., 2009; Sowers et al., 2019; Baken et al., 2013; Gault et al., 2012; Elliott and Warren, 2014; Rhoton et al., 2002; Emerson and Weiss, 2004; Gault et al., 2011; Isaacson et al., 2009; Mitsunobu et al., 2012), and the presence of ferrihydrite-like features in most of the XRD patterns (broad peaks centered around 2.54 and 1.49 Å, Fig. 3), we included a single PONKCS phase fitting 2-line ferrihydrite in our Rietveld fits. Further mineral phases were only considered in the QPA analysis when phases could be identified by the presence of a characteristic diffraction feature. Examples of the resulting Rietveld fits are shown for selected floc samples in Fig. S7 and XRD patterns of all flocs are shown in Fig. 3. Results from QPA analysis of all floc samples are detailed in Table S8 and show that floc samples comprised minor quantities of primary minerals such as augite, quartz, and plagioclase (<30%) and primarily consisted of poorly-crystalline minerals fitted as ferrihydrite (36–100%). In multiple floc samples, fractions of lepidocrocite (10–22%) were fit and, in floc sample F1, goethite (31%) was also fit. The fitted crystallite sizes for both of these fractions were <7 nm, respectively (LVol-IB, Double-Voigt approach fitting Cry size L in TOPAS), indicating that the minerals were nano-crystalline.

3.5. Floc Fe mineralogy: Fe K-edge X-ray absorption spectroscopy

To further investigate Fe speciation and mineralogy in the flocs, selected floc samples were additionally analyzed with Fe *K*-edge XAS. Linear combination fits of Fe *K*-edge XANES spectra provide information on Fe oxidation state in the flocs, and show that the Fe in all flocs was predominantly Fe(III) (Fig. S8, Table S9). In order to determine individual contributions of Fe species, we also performed LCF analyses of Fe *K*-edge EXAFS spectra. Data and model fits are shown in Fig. 4A, and fit parameters are detailed in Table 1. In good agreement with iron mineral phase contributions determined with XRD (Table S8), Fe in the flocs was found to comprise primarily ferrihydrite (33–72%), lepidocrocite (11–33%), and, in the case of F1, also goethite (27%). Additional contributions were found from organically-complexed Fe(III) (<10%), modelled by citrate- or oxalate-like Fe(III) complexes, phosphate-complexed Fe(III) (≤28%), and an Fe(III)-containing smectite (≤16%), fitted as nontronite Nau-2 with 19 wt% Fe.

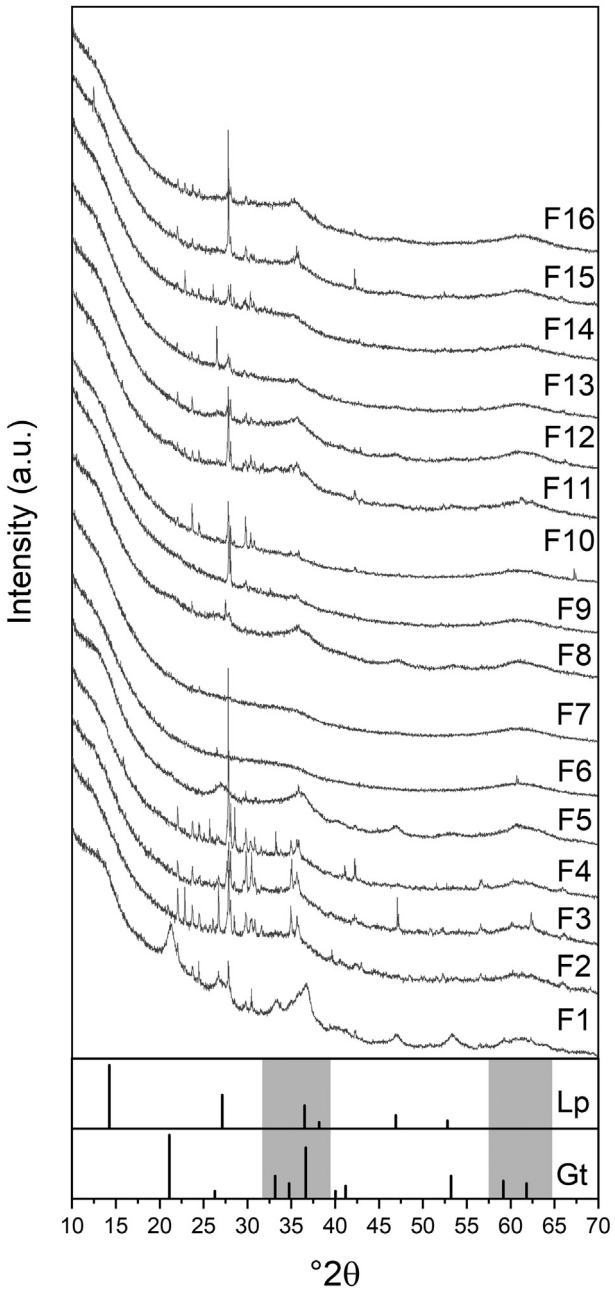

Fig. 3. X-ray diffraction patterns of floc samples and prominent features of reference spectra (Lp = lepidocrocite, Gt = goethite). Gray boxes centered around 2.54 and 1.49 Å indicate broad features typical of 2-line ferrihydrite. The sharp, crystalline peaks belong to plagioclase minerals, augite, and quartz. Rietveld fit parameters are detailed in Table S8 and examples of QPA analyses are shown in Fig. S7.

To explore the local coordination environment of Fe, we also performed shell-fit analyses of Fe *K*-edge EXAFS spectra. Spectra and model fits are shown in Fig. 4B, and details to fitted parameters are presented in Table 2. The first shell feature was similar in all spectra and was fit by an Fe-O path at ~1.99 Å, in agreement with octahedrally coordinated Fe atoms (Waychunas et al., 1993; Manceau, 2011). Fitted coordination numbers (CN) for the first shell ranged from 5.1 to 5.9, suggesting slight structural differences between the floc samples. Further differences were visible in second shell feature at 2.2–3.5 $R + \Delta R$ (Å), which primarily reflects scattering from neighboring Fe atoms in the second coordination shell. While all spectra were fit with an edge-sharing Fe-Fe_1 path at ~3.06 Å and a corner-sharing Fe-Fe_2 at 3.39–3.46 Å, variations in CNs and in the ratio of corner- to edge-

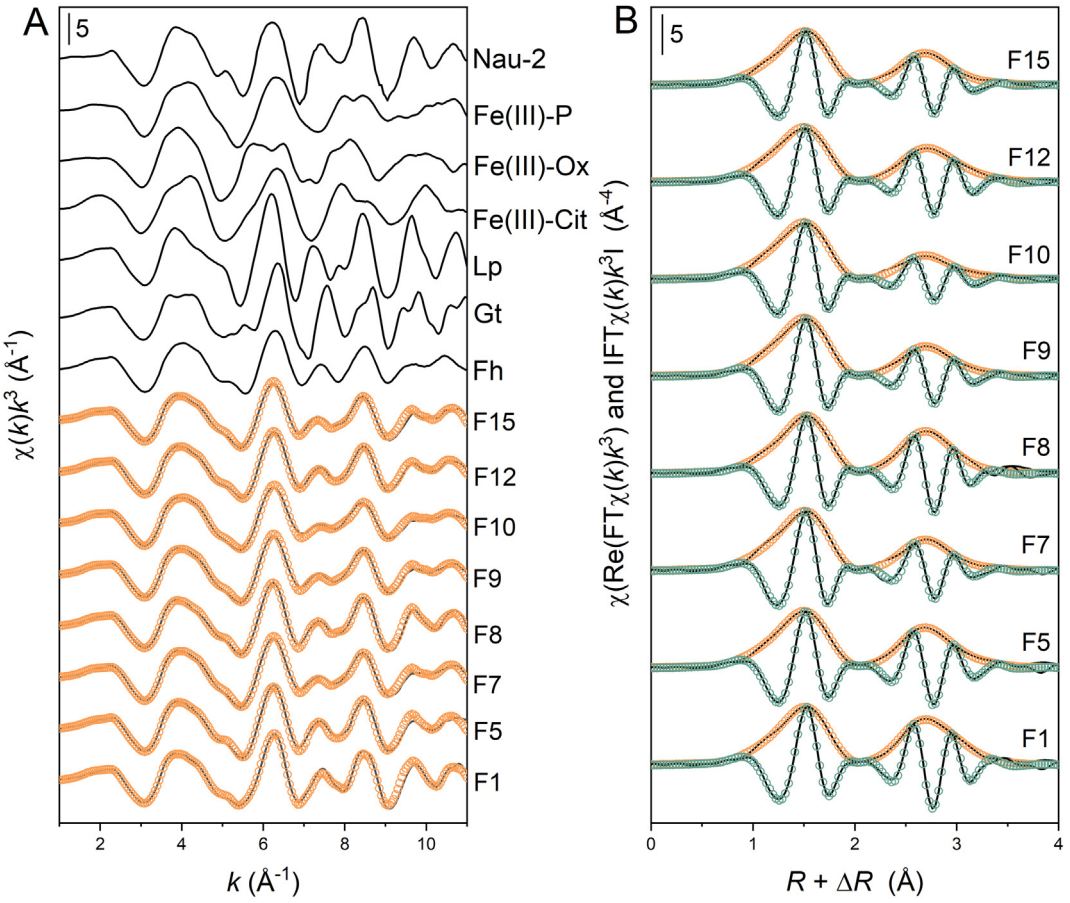

Fig. 4. (A) Iron *K*-edge EXAFS spectra of reference compounds, floc samples, and their linear combination fits (LCF). Experimental data and LCF are shown as solid lines and symbols, respectively. Fit results are reported in Table 1. (B) Iron *K*-edge Fourier-transform magnitudes and real parts of floc samples. Solid lines indicate experimental data and open circles show the model fits. Shell-fit parameters are reported in Table 2. Abbreviations: Fe(III)-Cit = Fe(III)-citrate, Fe(III)-Ox = Fe(III)-oxalate hexahydrate, Fe(III)-P = Fe(III)-phosphate dihydrate, Fh = ferrihydrite, Gt = goethite, Lp = lepidocrocite, Nau-2 = Fe-rich (19 wt%) nontronite.

sharing Fe (Fe-Fe_2/Fe-Fe_1) can indicate varying contributions from multiple Fe(III) (oxyhydr)oxides. For example, the nominal Fe-Fe_1 and Fe-Fe_2 CNs for lepidocrocite are 6 and 0, respectively (Zhukhlistov, 2001), whereas CNs of 1.3–2.9 ($\bar{x}$ = 1.8) and 1.4–3.1 ($\bar{x}$ = 2.2) for Fe-Fe_1 and Fe-Fe_2, respectively, and Fe-Fe_2/Fe-Fe_1 ratios of 0.96–1.86 ($\bar{x}$ = 1.26) have been reported for 2-line ferrihydrite (ThomasArrigo et al., 2019; Waychunas et al., 1993; Miot et al., 2009a). Therefore, both the higher edge-sharing Fe CNs (1.7–3.8) and lower Fe-Fe_2/Fe-Fe_1 ratios (0.52–1.04) confirm that the flocs primarily comprised a mixture of lepidocrocite and ferrihydrite.

Considering the C and P contents of the flocs (Table S3), and the organic- and phosphate-complexed Fe fractions determined with LCF analyses (Table 1), we also tried including an Fe-C path at R = 2.91–2.96 Å; distances in agreement with 5- and 6-membered chelate rings structures (Karlsson and Persson, 2010; Karlsson and Persson, 2012; Karlsson et al., 2008; Persson and Axe, 2005), and an Fe-P at R = 3.22–3.28 Å, representing expected path distances fit for amorphous ferric phosphates (Miot et al., 2009a; Baumgartner et al., 2013; Miot et al., 2009b). While both paths could be individually included (i.e. resulting fit parameters were reasonable), a statistical analysis

Table 1
Linear combination fit results for Fe *K*-edge EXAFS spectra of floc samples.

Sample	Fh (%)	Lp (%)	Gt (%)	Fe(III)-citrate/oxalate (%)	Fe(III)-phosphate (%)	Nau-2 (%)	NSSR[a] (%)	red. χ^{2}[b] (−)
F1	33	32	27	0/8	0	0	1.19	0.003
F5	64	20	0	0/0	0	16	1.53	0.004
F7	53	19	0	0/0	28	0	1.07	0.003
F8	47	33	0	9/0	0	11	0.78	0.002
F9	53	19	0	8/0	19	0	0.94	0.022
F10	55	11	0	9/0	24	0	1.14	0.003
F12	72	18	0	0/0	10	0	0.67	0.002
F15	53	24	0	0/0	23	0	0.01	0.003

Abbreviations: Fh = ferrihydrite, Lp = lepidocrocite, Gt = goethite, Nau-2 = nontronite.
[a] NSSR: Normalized sum of squared residuals ($100 \times \sum_i(\text{data}_i\text{-fit}_i)^2/\sum_i\text{data}^2$).
[b] Fit accuracy (reduced $\chi^2 = (N_{idp}/N_{pts})\sum_i((\text{data}_i\text{-fit}_i)/\varepsilon_i)^2(N_{idp}\text{-}N_{var})^{-1}$. N_{idp}, N_{pts} and N_{var} are, respectively, the number of independent points in the model fit (16), the total number of data points (201), and the number of fit variables (2–4). ε_i is the uncertainty of the *i*th data point (Kelly et al., 2008).

Table 2
Shell-fit parameters determined from Fe *K*-edge EXAFS spectra of floc samples.[a]

Sample	Fe-O			Fe-Fe_1		Fe-Fe_2		Fe-Fe_2/[e] Fe-Fe_1	ΔE_0[f]	NSSR[g]	red. χ^{2}[h]
	CN[b]	*R* (Å)[c]	σ^{2}[d]	*CN*	*R* (Å)	*CN*	*R* (Å)		(eV)	(%)	(−)
F1	5.9 (5)	1.99 (1)	0.010	3.8 (3)	3.06 (1)	3.9 (6)	3.39 (1)	1.03	−3.54 ± 1.01	0.6	247
F5	5.9 (4)	1.99 (1)	0.010	3.0 (3)	3.05 (1)	2.3 (5)	3.44 (1)	0.77	−3.55 ± 0.83	0.4	113
F7	5.6 (5)	1.99 (1)	0.009	2.3 (2)	3.07 (1)	1.2 (7)	3.44 (1)	0.52	−3.18 ± 1.12	1.0	427
F8	5.2 (5)	2.00 (1)	0.008	3.5 (2)	3.07 (1)	1.9 (6)	3.40 (2)	0.54	−2.43 ± 1.06	0.8	333
F9	5.7 (4)	1.99 (1)	0.010	2.2 (3)	3.06 (1)	1.5 (5)	3.44 (1)	0.68	−3.59 ± 0.91	0.6	490
F10	5.8 (5)	1.98 (1)	0.010	1.7 (2)	3.06 (1)	1.3 (5)	3.46 (3)	0.76	−3.73 ± 0.99	0.8	221
F12	5.7 (5)	1.98 (1)	0.010	2.5 (2)	3.06 (1)	2.6 (6)	3.44 (1)	1.04	−3.49 ± 1.08	0.8	725
F15	5.1 (4)	1.99 (1)	0.009	2.4 (3)	3.06 (1)	1.3 (5)	3.45 (3)	0.54	−3.19 ± 0.98	0.7	157

[a] The passive amplitude reduction factor, S_0^2, was set to 0.8. Parameter uncertainties in parenthesis are shown for the last significant figure. The Debye-Waller parameters, σ^2, were fixed to 0.008 Å^2 (Fe-Fe_1) and 0.014 Å^2 (Fe-Fe_2).
[b] Path degeneracy (coordination number).
[c] Mean half path length.
[d] Debye-Waller parameter.
[e] CN ratio between Fe-Fe_2 and Fe-Fe_1.
[f] Energy-shift parameter.
[g] Normalized sum of squared residuals ($100\sum_i(data_i\text{-}fit_i)^2/\sum_i data^2$).
[h] Fit accuracy; reduced $\chi^2 = (N_{idp}/N_{pts})\sum_i((data_i\text{-}fit_i)/\varepsilon_i)^2(N_{idp}\text{-}N_{var})^{-1}$. N_{idp}, N_{pts} and N_{var} are, respectively, the number of independent points in the model fit (15.7), the total number of data points (201), and the number of fit variables (8). ε_i is the uncertainty of the *i*th data point. *Note*: Models also included a triangular Fe-O-O multiple scattering path constrained as follows: $N = 4CN_{Fe\text{-}O}$, $R = R_{Fe\text{-}O}(1+\sqrt{2}/2)$, and $\sigma^2 = 2\sigma^2_{Fe\text{-}O}$ (ThomasArrigo et al., 2014; Mikutta, 2011).

revealed that neither path significantly improved the fit (*F*-tests (Downward et al., 2007), Supporting Information, Section 7), therefore neither path was included in the final fits. Discerning contributions from low Z backscattering atoms (e.g., C, P) during shell-fit analyses can be difficult when multiple or high Z backscattering atoms (e.g., Fe) are positioned in coordination shells at similar interatomic distances. Wavelet transform (WT) analyses can therefore provide additional information, as it resolves data in both *k*-space (Å^{-1}) and interatomic distance (*R*-space, Å) (Funke et al., 2005). Overview Morlet WTs of floc samples and references are shown in Fig. S9, where a distinct feature at R = 1–2 Å and k = 2 to 8 Å^{-1}, present in all floc samples and references, corresponds to Fe-O paths in the first coordination shell. In the *R*-range of 2.0–3.5 Å, differences are visible in higher coordination shell backscatterers of reference samples (Fig. S9). For the ferrihydrite, goethite, lepidocrocite, and Nau-2 references, backscatterers in the second coordination shell appear at k = 6 to 10 Å^{-1}, whereas the WT features in the in the Fe(III)-phosphate, Fe(III)-oxalate, and Fe(III)-citrate references appear at lower energy; k = 2 to 6 Å^{-1}. With high resolution Morlet WTs, differences between high and low Z backscatterers in the second coordination shell are more visible (Fig. 5). At high resolution, WTs of ferrihydrite, goethite, and lepidocrocite, are dominated by a strong signal from Fe backscatterers at R = 2.2–3.0 Å and k = 6 to 8 Å^{-1}. This feature results from edge- and corner-sharing Fe (ThomasArrigo et al., 2019; Zhukhlistov, 2001; Waychunas et al., 1993; Miot et al., 2009a) and is most intense in lepidocrocite and goethite, whereas the signal in ferrihydrite is weaker. For nontronite, second coordination shell signals may result from Fe-Fe, -Al, or -Si paths (O'Day et al., 2004). However, the similar position of this feature at ~7 Å^{-1} in the 19 wt% Fe Nau-2 reference suggests that it most likely reflects Fe backscatterers. The signal at R = 2.2–3.0 Å and k = 6 to 8 Å^{-1} is weakly visible in the Fe(III)-citrate reference, suggesting the presence of Fe in the second coordination shell, possibly present as polynuclear Fe (III)-citrate complexes (Mikutta et al., 2010). In contrast, the feature is completely absent from the Fe(III)-phosphate and Fe(III)-oxalate references. Instead, new signals at R = 2.2–2.7 Å and 3.0–3.3 Å and at lower energy ($k \leq 4$ Å^{-1}) are visible, in agreement with backscattering from P atoms in amorphous Fe(III)-phosphates (Miot et al., 2009a; Miot et al., 2009b) and from C and O atoms in higher coordination shells of tris (oxalato)iron(III) (Karlsson et al., 2008; Wartchow, 1997), respectively.

As Fig. 5 shows, WTs of floc samples were generally similar, whereby all floc samples were dominated by a prominent feature at R = 2.2–3.0 Å and k = 6 to 8 Å^{-1}, consistent with the presence of Fe backscatters in higher coordination shells. The WT maps are presented on the same color scale, therefore comparisons of relative contributions of Fe backscatters can be qualitatively assessed. As such, it is clear that floc samples F1, F5, and F8 have more intense maxima near 7 Å^{-1}. This finding is in agreement with both XRD and LCF analyses, which found higher contributions of the strong Fe-backscattering references (e.g., lepidocrocite, goethite, and nontronite) in these samples compared to the other floc samples (44–59% vs. 11–24% (LCF; Table 1) and 22–53% vs. 10–21% (XRD QPA; Table S8) for floc samples F1, F5, and F9 versus floc samples F7, F9, F10, F12, and F15, respectively). In addition to this, for some floc samples, a signal at R = 2.2–2.7 Å and k = 2 to 4 Å^{-1} is visible. This is particularly true for floc samples F7 and F10, and the feature is weakly visible in F9 and F15 (Fig. 5). The occurrence of this signal at lower energy suggests that these samples contain a low Z backscattering atom, and the position of the signal is similar to P backscattering in the Fe(III)-phosphate reference. Distinct features relating to C or distant O paths in Fe(III)-citrate or Fe(III)-oxalate could not be verified. These features may become more visible through modifying the WT parameters (κ or σ) (Giannetta et al., 2020); however, based on LCF analyses, contributions from C or O resulting from Fe (III)-organic complexes are expected to be low (<10%, Table 1). Collectively, WTs analyses qualitatively confirm results from both XRD and LCF analyses, suggesting that the flocs are dominated by Fe(III) (oxyhydr)oxides with occasional contributions from low Z atoms like P.

3.6. Floc Fe mineralogy: ^{57}Fe Mössbauer spectroscopy

Selected floc samples were additionally analyzed with ^{57}Fe Mössbauer spectroscopy. At 77 K, all samples displayed characteristics of poorly crystalline Fe minerals, with the majority of the spectral area fit by a paramagnetic doublet with center shift (CS; 0.47 mm s^{-1}) consistent with Fe(III) (Fe(III)-D1, Fig. S10). Floc sample F1 also presented a magnetically ordered sextet at 77 K (CS of 0.48 mm s^{-1}, mean quadrupole shift of −0.12 mm s^{-1}, and hyperfine field 46.7 T); parameters which are consistent with goethite with moderate crystallinity (Vandenberg and De Grave, 2013; Cornell and Schwertmann, 2003) and are in good agreement with goethite contributions detected in this sample with both XRD (Fig. 3) and Fe *K*-edge XAS (Fig. 4, Table 1). All fit parameters for 77 K measurements are presented in Table S13. At 4.2 K, all spectra comprised asymmetric sextets that required at least two sextets to produce a satisfactory fit (Fig. 6, Table 3). The first sextet, Fe(III)-S1, presented CS (0.46–0.49 mm s^{-1}) and quadrupole shift (−0.01 to −0.05 mm s^{-1}) values consistent with ferrihydrite (Cornell and Schwertmann, 2003; Murad, 1988). The average hyperfine field values for the Fe(III)-S1 sextet (47.9 ± 0.5 T) are also in agreement with expected parameters for two- and 6-line ferrihydrite (45–50 T)

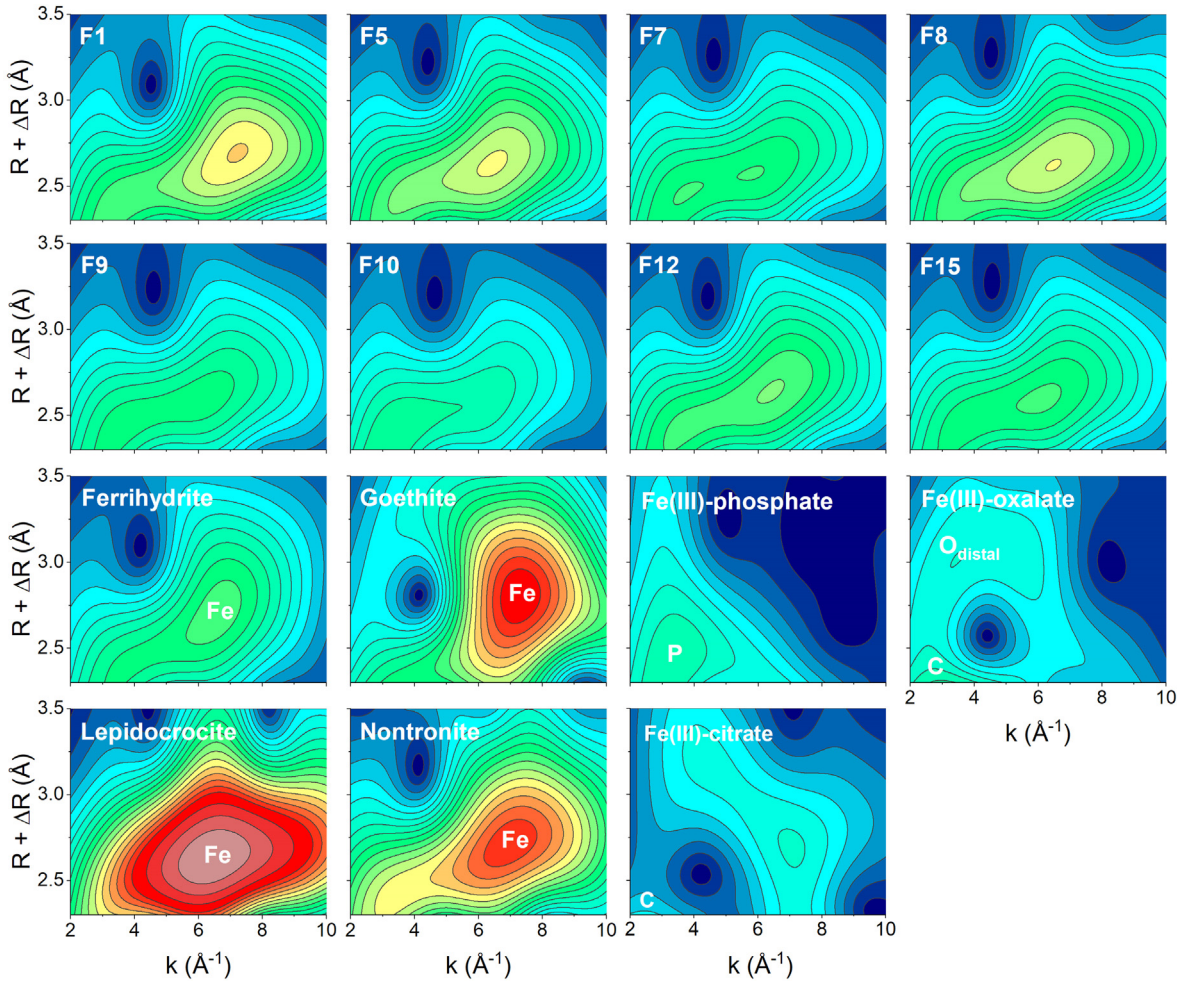

Fig. 5. High resolution Morlet wavelet transforms (WT) of k^2-weighted Fe *K*-edge EXAFS spectra of selected floc samples and reference spectra. The wavelet transforms were calculated over $R + \Delta R = 2.3–3.5$ Å ($\kappa = 4, \sigma = 2$).

(Eusterhues et al., 2008; Mikutta et al., 2008; Cornell and Schwertmann, 2003; Murad, 1988). Despite the relatively high C:Fe molar ratios in the studied flocs (0.4–2.4), the hyperfine field values are noticeably higher than hyperfine field parameters fit for ferrihydrite synthesized in the presence of or strongly associated to organic matter (40.8–46.0 T) (Eusterhues et al., 2008; ThomasArrigo et al., 2014). For the second sextet, Fe(III)-S2, the positive quadrupole shift (0.00 to 0.01 mm s^{-1}) and smaller hyperfine field (42.3 to 43.4 T) are in agreement with parameters reported for poorly crystalline lepidocrocite (Cornell and Schwertmann, 2003; Murad and Schwertmann, 1984) and are similar to lepidocrocite found in organic flocs from streambeds of a peatland (ThomasArrigo et al., 2014). It is important to note that distinction by Mössbauer spectroscopy between ferrihydrite and lepidocrocite in natural samples is difficult in view of ferrihydrite's broad lines. For these samples, the decision to add lepidocrocite to the fit was based on the asymmetry of the sextets and complimentary results from XRD and Fe *K*-edge EXAFS spectra. In floc sample F1, a separate sextet (Fe(III)-S3) was fit with parameters consistent with goethite (Murad, 1998) (CS of 0.48 mm s^{-1}, quadrupole shift of −0.11, mean hyperfine field 49.6 T).

While the magnetically ordered sextets of species Fe(III)-S1, Fe(III)-S2, and Fe(III)-S3 accounted for more than 85% of the spectra, additional features were necessary to provide a more accurate fit of the 4.2 K spectra (Fig. 6). Floc samples F1, F10, and F12 presented a small paramagnetic doublet (Fe(III)-D2) with CS (0.44 to 0.50 mm s^{-1}) and quadrupole split (0.67 to 0.82 mm s^{-1}), likely from Fe(III) complexed with organic matter (ThomasArrigo et al., 2014; Zhao et al., 2020; Thompson et al., 2011). Floc sample F5 presented a broad sextet with a hyperfine field of 38.3 T (Fe(III)-S4), which is considered small for most natural Fe (oxyhydr)oxides. Nontronites undergoing magnetic ordering can present a magnetic component (Baron et al., 2017). Thus, based on the Nau-2 fraction fitted in LCF analyses of Fe *K*-edge EXAFS spectra (Table 1), it seems most likely that Fe(III)-S4 corresponds to an Fe(III)-containing clay mineral. Finally, samples F7, F10, ad F12 present a poorly-ordered magnetic sextet (CF). Similar semi-collapsed features have been associated with Fe(III) associated with carbon or Fe in nanometer-sized Fe(III) (oxyhydr)oxides (Eusterhues et al., 2008; Zhao et al., 2020; Schwertmann et al., 2005). However, this feature also resembles the collapsed sextet collected for commercial Fe(III)-phosphate dihydrate ($FePO_4 \cdot 2H_2O$, Sigma-Aldrich) at 4.2 K (Fig. S11). Because the fitting parameters of the collapsed sextet are not sufficient to accurately assign a mineral phase, we can only suggest that the collapsed phase found with Mössbauer spectroscopy may correspond to organic-associated Fe(III), or may represent Fe(III)-phosphate complexes similarly fit during LCF analyses of Fe *K*-edge EXAFS spectra (Table 1) and qualitatively identified with WT analyses (Fig. 5). A summary table comparing (mineral) phases fit by each analysis (XRD, XAS, and Mössbauer) is presented in the Supporting Information (Table S14).

3.7. Iceland floc Fe mineral formation

While poorly crystalline, ferrihydrite-like phases are often reported to dominate Fe mineralogy of flocs or BIOS (Cockell et al., 2011; Ferris et al., 2000; Ferris et al., 1999; Sowers et al., 2017; Whitaker and Duckworth, 2018; Field et al., 2019; Kennedy et al., 2011; Langley

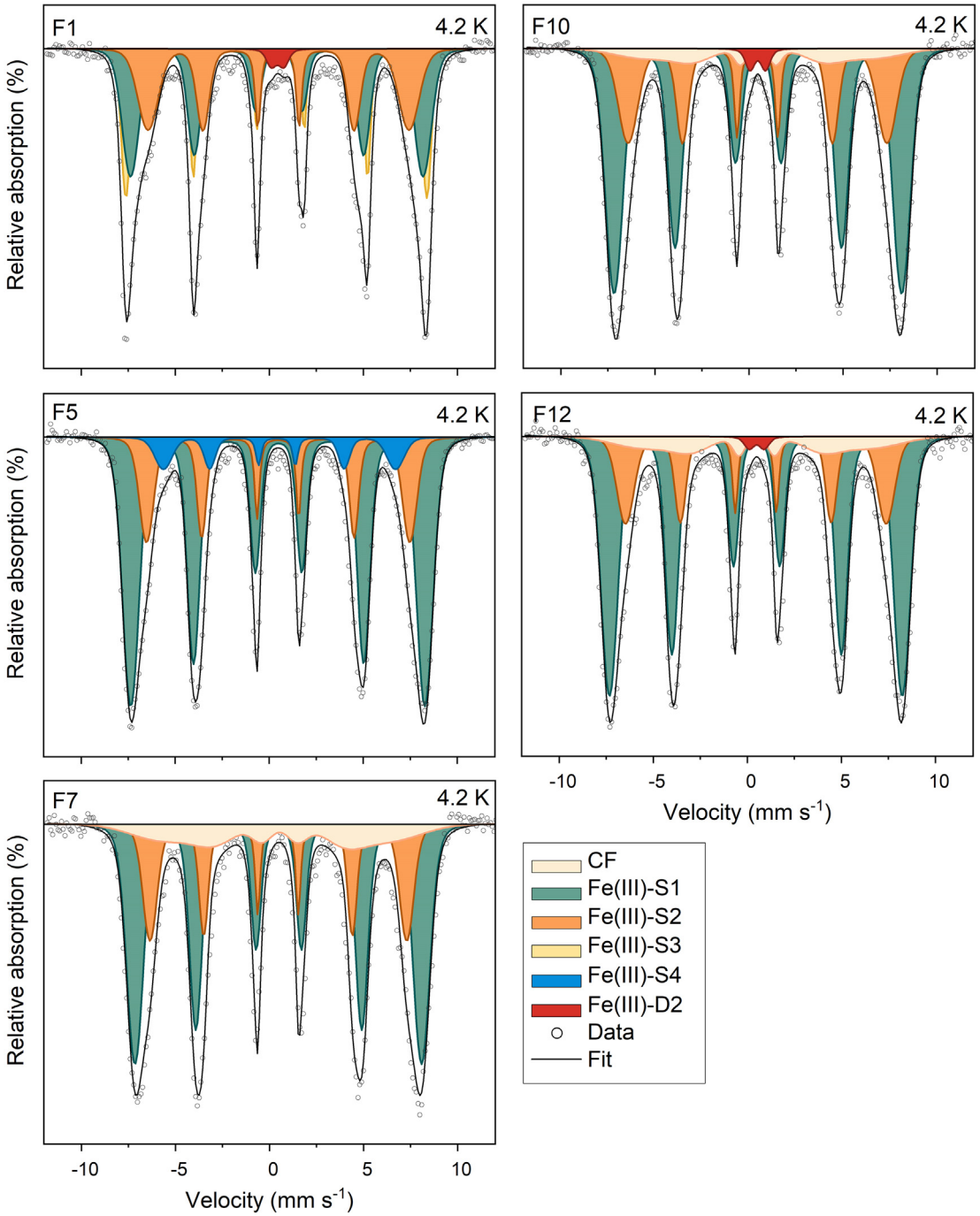

Fig. 6. Mössbauer spectra and fits of selected floc samples collected at 4.2 K. Fit parameters are presented in Table 3. Species assignments: Fe(III)-S1 = ferrihydrite, Fe(III)-S2 = lepidocrocite, Fe(III)-S3 = goethite, Fe(III)-S4 = Fe in clays, Fe(III)-D2 = Fe(III) associated to organic matter, CF = collapsed feature. Fit parameters are detailed in Table 3.

et al., 2009; Sowers et al., 2019; Baken et al., 2013; Gault et al., 2012; Elliott and Warren, 2014; Rhoton et al., 2002; Emerson and Weiss, 2004; Gault et al., 2011; Isaacson et al., 2009; Mitsunobu et al., 2012), the presence of nanometer-sized crystalline iron minerals (e.g., lepidocrocite and goethite), like those found in the Iceland flocs, have been previously reported for flocs or BIOS in a multitude of natural environments (ThomasArrigo et al., 2014; Gault et al., 2012; Rhoton et al., 2002; Gault et al., 2011; Isaacson et al., 2009). In redox dynamic wetland environments, formation and growth of floc Fe minerals is likely driven by both abiotic mechanisms as well as biogenic iron(III) mineral formation by iron(II)-oxidizing bacteria. The likelihood of the latter is confirmed through microscope images identifying sheaths and stalks indicative of both *Leptothrix* spp. and *Gallionella* spp., respectively (Figs. S3, S4, and S5), in agreement with microscopy and 16S rRNA analyses performed by Cockell et al. on similar microbial mat precipitates from Iceland (Cockell et al., 2011). In laboratory studies, reported mineral products of Fe(II) oxidation by cultivated *Leptothrix* spp. include ferrihydrite, lepidocrocite, goethite, and magnetite (Angelova et al., 2015; Vollrath et al., 2013; Nedkov et al., 2016). Furthermore, in the Iceland flocs, it is possible that the generally cold water temperature (~10 °C, Table S1) promoted microbially-derived lepidocrocite formation over ferrihydrite (Vollrath et al., 2013).

However, sheaths and stalks indicative of *Leptothrix* spp. and *Gallionella* spp. varied in abundance among the imaged floc samples (compare floc samples F9 and F10, Fig. S3) with no evidence of sheaths or stalks seen in floc sample F6 (Fig. S3). Therefore, it seems likely that

Table 3
Mössbauer parameters of selected floc samples measured at 4.2 K.

Sample	Species	CS[a]	QS[b]	<|H|>[c]	Population	red. χ^2[d]
		(mm s^{-1})	(mm s^{-1})	(T)	(%)	(−)
F1	Fe(III)-S1[e]	0.46	−0.05	48.2	40.3	1.27
	Fe(III)-S2	0.49	0.00	43.0	30.3	
	Fe(III)-S3	0.48	−0.11	49.6	27.7	
	Fe(III)-D2	0.44	0.67		1.7	
F5	Fe(III)-S1	0.48	−0.02	48.5	68.1	2.24
	Fe(III)-S2	0.47	0.01	43.4	23.4	
	Fe(III)-S4	0.48	0.07	38.3	8.4	
F7	Fe(III)-S1	0.48	−0.01	47.3	59.7	1.42
	Fe(III)-S2	0.46	0.01	42.3	25.4	
	CF	0.45	−0.09	37.2	14.9	
F10	Fe(III)-S1	0.49	−0.01	47.4	63.1	2.05
	Fe(III)-S2	0.45	0.00	42.7	26.6	
	CF	0.50	0.01	37.0	8.7	
	Fe(III)-D2	0.46	0.82		1.6	
F12	Fe(III)-S1	0.47	−0.02	48.3	65.7	1.06
	Fe(III)-S2	0.45	0.01	42.9	22.9	
	CF	0.50	0.00	37.0	10.5	
	Fe(III)-D2	0.50	0.81		0.9	

[a] Center shift.
[b] Quadrupole splitting for doublets and quadrupole shift parameter for sextets.
[c] Hyperfine field.
[d] Fit accuracy.
[e] Species assignments: Fe(III)-S1 = ferrihydrite, Fe(III)-S2 = lepidocrocite, Fe(III)-S3 = goethite, Fe(III)-S4 = Fe in clays, Fe(III)-D2 = organically-complexed Fe, CF = collapsed feature potentially representing organic or phosphate-complexed Fe.

abiotic Fe(II) oxidation and precipitation processes and microbial Fe(II) oxidation were simultaneously active. For example, lepidocrocite may have formed abiotically through slow oxidation of Fe(II) facilitated by low pO_2 (Schwertmann and Cornell, 2000). Owing to the high mobility of flocs (Fig. S1), it is unlikely that growth of more crystalline phases (e.g., goethite) occurred through ageing of (a)biotically produced ferrihydrite, as this process occurs over significantly longer timescales (e.g., months to years) at circumneutral pH and lower temperatures (Schwertmann et al., 2004). Rather, goethite may have formed spontaneously, as cold (10 °C) natural waters in Iceland have been reported to be (super) saturated with respect to goethite (Stefánsson and Gíslason, 2001), and was thereafter entrapped within the floc (organic) matrix. Alternatively, nanometer-sized secondary mineral phases, including lepidocrocite and goethite, may form during the rapid (timescale = days) abiotic Fe(II)-catalyzed transformation of the ferrihydrite in the presence of organic matter (ThomasArrigo et al., 2019; ThomasArrigo et al., 2018). With considerable dissolved Fe^{2+} detected in surface waters at all sites (Table S2), formation of lepidocrocite and goethite via this pathway seems plausible. Additionally, the coexistence of both FeOB and FeRB reported in Iceland microbial mat samples (Cockell et al., 2011) and other flocs or BIOS (Cockell et al., 2011; Gault et al., 2012; Elliott and Warren, 2014; Gault et al., 2011; Elliott et al., 2014) suggests microbial Fe cycling may be important, with both biotically-derived and entrapped mineral phases serving as sources of Fe(III).

4. Conclusions

This work examines the complex interactions between (microbially-derived) organic matter, particulate mineral phases, and (microbial) Fe cycling driving trace element sequestration and Fe mineral precipitation and growth in Fe-rich flocs collected from cold wetlands in Iceland. Using a combination of mineral analysis techniques (XRD, XAS, ^{57}Fe Mössbauer) and chemical extractions, we showed that the Iceland flocs comprise, in addition to ferrihydrite, appreciable amounts of nano-crystalline lepidocrocite and goethite, Fe in clay minerals, and poorly-crystalline aluminosilicates, most likely allophane or imogolite. In combination with the abundance of Fe in the flocs, floc (bio)organics likely facilitate the sorption of trace elements both directly, via sorption and/or complexation mechanisms, and indirectly, through providing a structure which entraps nanoparticulate inorganic phases and acts as nucleation sites for mineral precipitation.

Accumulations of bright orange (a)biogenic iron minerals are common occurrences in the Fe-rich wetlands of Iceland. However, their high mobility, the extensive drainage network impacting Iceland's lowland wetlands and their general proximity to the coast suggests that these flocs are likely to contribute to the suspended sediment load reaching coastal waters and thus are likely transport vectors contributing to the export of Fe, organic carbon, and floc-associated trace elements from wetlands. Iceland flocs were previously shown to contain both FeOB and FeRB (Cockell et al., 2011). However, exposure to varying geochemical conditions associated with coastal waters (i.e., higher ionic strength, presence of sea-water derived sulfate) or floc sedimentation and burial may lead to shifts in floc microbial communities, resulting in the (a)biotic reductive dissolution of the poorly-crystalline floc Fe phases. The high fraction of floc-trace elements extracted by hydroxylamine hydrochloride suggests that, in addition to dissolved Fe, the reductive dissolution of floc Fe phases may lead to the release of trace elements and organic carbon. Thus, Iceland flocs appear to have the capacity to sequester trace elements or organic carbon for short-term durations. In terms of long-term storage and efficacy, however, future studies could investigate the biogeochemical stability of Fe phases and associated trace elements in Iceland flocs.

CRediT authorship contribution statement

Laurel K. ThomasArrigo: Conceptualization, Methodology, Investigation, Visualization, Writing – original draft. **Luiza Notini:** Investigation, Writing – review & editing. **Jeremiah Shuster:** Investigation, Writing – review & editing. **Tabea Nydegger:** Investigation, Writing – review & editing. **Sophie Vontobel:** Investigation, Writing – review & editing. **Stefan Fischer:** Investigation, Writing – review & editing. **Andreas Kappler:** Writing – review & editing. **Ruben Kretzschmar:** Writing – review & editing.

Declaration of competing interest

The authors declare that they have no known competing financial interests or personal relationships that could have appeared to influence the work reported in this paper.

Acknowledgements

We are grateful to K. Barmettler, P. Kälin, and S. Bouchet (ETH Zurich) for assisting with laboratory analyses, and X. Fang (ETH Zurich), J. Mayerhofer (Agroscope), Ó. Arnalds and H. Óskarsson (Agricultural University of Iceland, AUI) for helpful discussions and the AUI for providing accommodation during field campaigns, and the Icelandic Meteorological Office for providing precipitation data. We acknowledge SOLEIL (Proposal no. 20200766) for the provision of synchrotron radiation facilities and thank G. Landrot (SAMBA beamline) for support during the synchrotron measurements. This project has received funding from the Swiss Polar Institute and BNP Paribas Swiss Foundation (L. ThomasArrigo, PAF-2020-03), an ETH Career Seed Grant (L. ThomasArrigo, SEED-13 18-2), and received funding from the European Research Council (ERC) under the European Union's Horizon 2020 research and innovation programme (R. Kretzschmar, Grant agreement No. 788009-IRMIDYN-ERC-2017-ADG) and ETH Zurich. We also thank the German Research Foundation DFG (INST 37/1027-1 FUGG) for financial support provided for the acquisition of the cryogenic focused ion beam scanning electron microscope used in this study at University Tübingen.

Appendix A. Supplementary data

Details to field site locations and floc characterization, supplemental elemental, XRD, XAS, and ^{57}Fe Mössbauer data. This information is

available free of charge via the Internet at http://pubs.acs.org/. Supplementary data to this article can be found online at https://doi.org/10.1016/j.scitotenv.2021.151567.

References

Angelova, R., Groudeva, V., Slavov, L., Iliev, M., Nedkov, I., Sziklai-László, I., Krezhov, K., 2015. Investigation of iron-containing products from natural and laboratory cultivated Sphaerotilus-Leptothrix bacteria. J. Biol. Phys. 41, 367–375.

Arnalds, O., 2010. Dust sources and deposition of aeolian materials in Iceland. Icel. Agric. Sci. 23, 3–21.

Arnalds, O., 2015. The Soils of Iceland. Springer Science+Business Media.

Arnalds, O., Hallmark, C.T., Wilding, L.P., 1995. Andisols from four different regions of Iceland. Soil Sci. Soc. Am. J. 59, 161–169.

Arnalds, O., Gudmundsson, J., Oskarsson, H., Brink, S.H., Gisladottir, F.O., 2016. Icelandic inland wetlands: characteristics and extent of draining. Wetlands 36 (4), 759–769.

Arnórsson, S.N., Gunnarsson, I., Stefánsson, A., Andrésdóttir, A., Sveinbjörnsdóttir, A.E., 2002. Major element chemistry of surface- and ground waters in basaltic terrain, N-Iceland. I. Primary mineral saturation. Geochim. Cosmochim. Acta 66, 4015–4046.

Artz, R.R.E., Chapman, S.J., Robertson, A.H.J., Potts, J.M., Laggoun-Défarge, F., Gogo, S., Comont, L., Disnar, J.-R., Francez, A.-J., 2008. FTIR spectroscopy can be used as a screening tool for organic matter quality in regenerating cutover peatlands. Soil Biol. Biochem. 40, 515–527.

Baken, S., Sjöstedt, C., Gustafsson, J.P., Seuntjens, P., Desmet, N., De Schutter, J., Smolders, E., 2013. Characterisation of hydrous ferric oxides derived from iron-rich groundwaters and their contribution to the suspended sediment of streams. Appl. Geochem. 39, 59–68.

Baron, F., Petit, S., Pentrák, M., Decarreau, A., Stucki, J.W., 2017. Revisiting the nontronite Mössbauer spectra. Am. Miner. 102, 1501–1515.

Baumgartner, J., Morin, G., Menguy, N., Gonzalez, T.P., Widdrat, M., Cosmidis, J., Faivre, D., 2013. Magnetotactic bacteria form magnetite from a phosphate-rich ferric hydroxide via nanometric ferric (oxyhydr)oxide intermediates. 110, 14883–14888.

Bishop, J.L., Rampe, E.B., Bish, D.L., Abidin, Z., Baker, L.L., Matsue, N., Henmi, T., 2013. Spectral and hydration properties of allophane and imogolite. Clay Clay Miner. 61, 57–74.

Buliauskaitė, R., Wilfert, P., Kumar, P.S., de Vet, W., Witkamp, G.J., Korving, L., van Loosdrecht, M.C.M., 2020. Biogenic iron oxides for phosphate removal. Environ. Technol. 41, 260–266.

Carlile, M.J., Dudeney, A.W.L., 2000. A microbial mat composed of iron bacteria. Microbiology 146, 2092–2093.

Carlson, L., Schwertmann, U., 1981. Natural ferrihydrites in surface deposits from Finland and their association with silica. Geochim. Cosmochim. Acta 45, 421–429.

Chan, C.S., De Stasio, G., Welch, S.A., Girasole, M., Frazer, B.H., Nesterova, M.V., Fakra, S., Banfield, J.F., 2004. Microbial polysaccharides template assembly of nanocrystal fibers. Science 303, 1656–1658.

Chan, C.S., Fakra, S.C., Edwards, D.C., Emerson, D., Banfield, J.F., 2009. Iron oxyhydroxide mineralization on microbial extracellular polysaccharides. Geochim. Cosmochim. Acta 73, 3807–3818.

Cockell, C.S., Kelly, L.C., Summers, S., Marteinsson, V., 2011. Following the kinetics: iron-oxidizing microbial mats in cold icelandic volcanic habitats and their rock-associated carbonaceous signature. Astrobiology 11, 679–694.

Cornell, R.M., Schwertmann, U., 2003. The Iron Oxides: Structure, Properties, Reactions, Occurances and Uses. Wiley-VCH, Weinheim, Germany.

Dahlgren, R.A., 1994. Quantification of allophane and imogolite. In: Amonette, J.E., Zelanzy, L.W. (Eds.), Quantitative Methods in Soil Mineralogy. Soil Science Society of America, Madison, WI, USA, pp. 430–451.

Davison, W., Seed, G., 1983. The kinetics of the oxidation of ferrous iron in synthetic and natural waters. Geochim. Cosmochim. Acta 47, 67–79.

Downward, L., Booth, C.H., Lukens, W.W., Bridges, F., 2007. A variation of the F-test for determining statistical relevance of particular parameters in EXAFS fits. AIP Conf. Proc. 882, 129–131.

Droppo, I.G., 2001. Rethinking what constitutes suspended sediment. Hydrol. Process. 15, 1551–1564.

Druschel, G.K., Emerson, D., Sutka, R., Suchecki, P., Luther, G.W., 2008. Low-oxygen and chemical kinetic constraints on the geochemical niche of neutrophilic iron(II) oxidizing microorganisms. Geochim. Cosmochim. Acta 72, 3358–3370.

Elliott, A.V.C., Warren, L.A., 2014. Microbial engineering of floc Fe and trace metal geochemistry in a circumneutral, remote lake. Environ. Sci. Technol. 48, 6578–6587.

Elliott, A.V.C., Plach, J.M., Droppo, I.G., Warren, L.A., 2012. Comparative floc-bed sediment trace element partitioning across variably contaminated aquatic ecosystems. Environ. Sci. Technol. 46, 209–216.

Elliott, A.V.C., Plach, J.M., Droppo, I.G., Warren, L.A., 2014. ollaborative microbial Fe-redox cycling by pelagic floc bacteria across wide ranging oxygenated aquatic systems. Chem. Geol. 366, 90–102.

Elzinga, E.J., Huang, J.H., Chorover, J., Kretzschmar, R., 2012. ATR-FTIR spectroscopy study of the influence of pH and contact time on the adhesion of Shewanella putrefaciens bacterial cells to the surface of hematite. Environ. Sci. Technol. 46, 12848–12855.

Emerson, D., Weiss, J.V., 2004. Bacterial iron oxidation in circumneutral freshwater habitats: findings from the field and the laboratory. Geomicrobiol J. 21, 405–414.

Emerson, D., Fleming, E.J., McBeth, J.M., 2010. Iron-oxidizing bacteria: an environmental and genomic perspective. Annu. Rev. Microbiol. 64, 561–583.

Eusterhues, K., Wagner, F.E., Häusler, W., Hanzlik, M., Knicker, H., Totsche, K.U., Kögel-Knabner, I., Schwertmann, U., 2008. Characterization of ferrihydrite-soil organic matter coprecipitates by X-ray diffraction and Mössbauer spectroscopy. Environ. Sci. Technol. 42, 7891–7897.

Ferris, F.G., Konhauser, K.O., Lyvén, B., Pedersen, K., 1999. Accumulation of metals by bacteriogenic iron oxides in a subterranean environment. Geomicrobiol J. 16, 181–192.

Ferris, F.G., Hallberg, R.O., Lyvén, B., Pedersen, K., 2000. Retention of strontium, cesium, lead and uranium by bacterial iron oxides from a subterranean environment. Appl. Geochem. 15, 1035–1042.

Field, H.R., Whitaker, A.H., Henson, J.A., Duckworth, O.W., 2019. Sorption of copper and phosphate to diverse biogenic iron (oxyhydr) oxide deposits. Sci. Total Environ. 697, 134111.

Fleming, E.J., Cetinić, I., Chan, C.S., King, D.W., Emerson, D., 2014. Ecological succession among iron-oxidizing bacteria. ISME J. 8, 804–815.

Fortin, D., Langley, S., 2005. Formation and occurrence of biogenic iron-rich minerals. Earth Sci. Rev. 72, 1–19.

Funke, H., Scheinost, A.C., Chukalina, M., 2005. Wavelet analysis of extended X-ray absorption fine structure data. Phys. Rev. B 71, 094110.

Gault, A.G., Ibrahim, A., Langley, S., Renaud, R., Takahashi, Y., Boothman, C., Lloyd, J.R., Clark, I.D., Ferris, F.G., Fortin, D., 2011. Microbial and geochemical features suggest iron redox cycling within bacteriogenic iron oxide-rich sediments. Chem. Geol. 281, 41–51.

Gault, A.G., Langley, S., Ibrahim, A., Renaud, R., Takahashi, Y., Boothman, C., Lloyd, J.R., Clark, I.D., Ferris, F.G., Fortin, D., 2012. Seasonal changes in mineralogy, geochemistry and microbial community of bacteriogenic iron oxides (BIOS) deposited in a circumneutral wetland. Geomicrobiol J. 29, 161–172.

Giannetta, B., Siebecker, M.G., Zaccone, C., Plaza, C., Rovira, P., Vischetti, C., Sparks, D.L., 2020. Iron(III) fate after complexation with soil organic matter in fine silt and clay fractions: an EXAFS spectroscopic approach. Soil Till. Res. 200, 104617.

Hao, L.K., Guo, Y., Byrne, J.M., Zeitvogel, F., Schmid, G., Ingino, P., Li, J.L., Neu, T.R., Swanner, E.D., Kappler, A., Obst, M., 2016. Binding of heavy metal ions in aggregates of microbial cells, EPS and biogenic iron minerals measured in-situ using metal- and glycoconjugates-specific fluorophores. Geochim. Cosmochim. Acta 180, 66–96.

Isaacson, L.S., Burton, E.D., Bush, R.T., Mitchell, D.R.G., Johnston, S.G., Macdonald, B.C.T., Sullivan, L.A., White, I., 2009. Iron(III) accumulations in inland saline waterways, Hunter Valley, Australia: mineralogy, micromorphology and pore-water geochemistry. Appl. Geochem. 24, 1825–1834.

Karlsson, T., Persson, P., 2010. Coordination chemistry and hydrolysis of Fe(III) in a peat humic acid studied by X-ray absorption spectroscopy. Geochim. Cosmochim. Acta 74, 30–40.

Karlsson, T., Persson, P., 2012. Complexes with aquatic organic matter suppress hydrolysis and precipitation of Fe(III). Chem. Geol. 322, 19–27.

Karlsson, T., Persson, P., Skyllberg, U., Mörth, C.-M., Giesler, R., 2008. Characterization of iron(III) in organic soils using extended X-ray absorption fine structure spectroscopy. Environ. Sci. Technol. 42, 5449–5454.

Kaur, N., Singh, B., Kennedy, B.J., Gräfe, M., 2009. The preparation and characterization of vanadium-substituted goethite: the importance of temperature. Geochim. Cosmochim. Acta 73, 582–593.

Kelly, S.D., Hesterberg, D., Ravel, B., 2008. Analysis of soils and minerals using X-ray absorption spectroscopy. In: Ulery, A.L., Drees, L.R. (Eds.), Methods of Soil Analysis. Part 5. Minerological Methods. Soil Science Society of America, Madison, pp. 378–463.

Kennedy, C.B., Gault, A.G., Fortin, D., Clark, I.D., Ferris, F.G., 2011. Retention of iodide by bacteriogenic iron oxides. Geomicrobiol J. 28, 387–395.

Kikuchi, S., Kashiwabara, T., Shibuya, T., Takahashi, Y., 2019. Molecular-scale insights into differences in the adsorption of cesium and selenium on biogenic and abiogenic ferrihydrite. Geochim. Cosmochim. Acta 251, 1–14.

Lagarec, K., Rancourt, D.G., 1997. Extended Voigt-based analytic lineshape method for determining N-dimensional correlated hyperfine parameter distributions in Mossbauer spectroscopy. 129, 266–280.

Langley, S., Gault, A.G., Ibrahim, A., Takahashi, Y., Renaud, R., Fortin, D., Clark, I.D., Ferris, F.G., 2009. Sorption of strontium onto bacteriogenic iron oxides. Environ. Sci. Technol. 43, 1008–1014.

Leppard, G.G., Droppo, I.G., West, M.M., Liss, S.N., 2003. Compartmentalization of metals within the diverse colloidal matrices comprising activated sludge microbial floes. J. Environ. Qual. 32, 2100–2108.

Loeppert, R.H., Inskeep, W.P., 1996. Iron. In: Sparks, D.L., Page, A.L., Helmke, P.A., Loeppert, R.H., Soltanpour, P.N., Tabatabai, M.A., Johnston, C.T., Sumner, M.E. (Eds.), Methods of Soil Analysis, Part 3. Chemical Methods. Soil Science Society of America, Madison, Wisconson, pp. 639–644.

Lovley, D.R., Phillips, E.J.P., 1987. Rapid assay for microbially reducible ferric iron in aquatic sediments. Appl. Environ. Microb. 53, 1536–1540.

Manceau, A., 2011. Critical evaluation of the revised akdalaite model for ferrihydrite. Am. Miner. 96, 521–533.

Martinez, R.E., Pedersen, K., Ferris, F.G., 2004. Cadmium complexation by bacteriogenic iron oxides from a subterranean environment. J. Colloid Interf. Sci. 275, 82–89.

McBeth, J.M., Fleming, E.J., Emerson, D., 2013. The transition from freshwater to marine iron-oxidizing bacterial lineages along a salinity gradient on the Sheepscot River, Maine,USA. 5, 453–463.

Mikutta, C., 2011. X-ray absorption spectroscopy study on the effect of hydroxybenzoic acids on the formation and structure of ferrihydrite. Geochim. Cosmochim. Acta 75, 5122–5139.

Mikutta, C., Mikutta, R., Bonneville, S., Wagner, F., Voegelin, A., Christl, I., Kretzschmar, R., 2008. Synthetic coprecipitates of exopolysaccharides and ferrihydrite. Part 1: characterization. Geochim. Cosmochim. Acta 72, 1111–1127.

Mikutta, C., Frommer, J., Voegelin, A., Kaegi, R., Kretzschmar, R., 2010. Geochim. Cosmochim. Acta 74, 5574–5592.

Miot, J., Benzerara, K., Morin, G., Kappler, A., Bernard, S., Obst, M., Férard, C., Skouri-Panet, F., Guigner, J.-M., Posth, N., Galvez, M., Brown, G.E., Guyot, F., 2009. Iron

biomineralization by anaerobic neutrophilic iron-oxidizing bacteria. Geochim. Cosmochim. Acta 73, 696–711.
Miot, J., Benzerara, K., Morin, G., Bernard, S., Beyssac, O., Larquet, E., Kappler, A., Guyot, F., 2009. Transformation of vivianite by anaerobic nitrate-reducing iron-oxidizing bacteria. Geobiology 7, 373–384.
Mitsunobu, S., Shiraishi, F., Makita, H., Orcutt, B.N., Kikuchi, S., Jorgensen, B.B., Takahashi, Y., 2012. Bacteriogenic Fe(III) (oxyhydr)oxides characterized by synchrotron microprobe coupled with spatially resolved phylogenetic analysis. Environ. Sci. Technol. 46, 3304–3311.
Murad, E., 1988. The Mössbauer spectrum of 'well'-crystallized ferrihydrite. J. Magn. Magn. Mater. 74, 153–157.
Murad, E., 1998. Clays and clay minerals: what can Mossbauer spectroscopy do to help understand them? Hyperfine Interact. 117 (1–4), 39–70.
Murad, E., Schwertmann, U., 1984. The influence of crystallinity on the Mössbauer spectrum of lepidocrocite. Mineral. Mag. 48, 507–511.
Nedkov, I., Slavov, L., Angelova, R., Blagoev, B., Kovacheva, D., Abrashev, M.V., Iliev, M., Groudeva, V., 2016. Biogenic nanosized iron oxides obtained from cultivation of iron bacteria from the genus Leptothrix. J. Biol. Phys. 42, 587–600.
O'Day, P.A., Rivera, N., Root, R., Carroll, S.A., 2004. Am. Miner. 89, 572–585.
Olafsson, H., Furger, M., Brummer, B., 2007. The weather and climate of Iceland. Meteorol. Z. 16 (1), 5–8.
Parikh, S.J., Chorover, J., 2006. ATR-FTIR spectroscopy reveals bond formation during bacterial adhesion to iron oxide. Langmuir 22, 8492–8500.
Perret, D., Gaillard, J.F., Dominik, J., Atteia, O., 2000. The diversity of natural hydrous iron oxides. Environ. Sci. Technol. 34, 3540–3546.
Persson, P., Axe, K., 2005. Adsorption of oxalate and malonate at the water-goethite interface: molecular surface speciation from IR spectroscopy. Geochim. Cosmochim. Acta 69, 541–552.
Plach, J.M., Warren, L.A., 2012. Differentiating natural organic matter roles in freshwater floc and bed sediment lead dynamics. Chem. Geol. 304, 97–105.
Plach, J.M., Elliott, A.V.C., Droppo, I.G., Warren, L.A., 2011. Physical and ecological controls on freshwater floc trace metal dynamics. Environ. Sci. Technol. 45, 2157–2164.
Plach, J.M., Lin, S., Droppo, I.G., Warren, L.A., 2014. Iron cycling in a littoral freshwater beach: implications for floc trace metal dynamics. J. Great Lakes Res. 40, 47–57.
Ravel, B., Newville, M., 2005. ATHENA, ARTEMIS, HEPHAESTUS: data analysis for X-ray absorption spectroscopy using IFEFFIT. J. Synchrotron Radiat. 12, 537–541.
Rentz, J.A., Turner, I.P., Ullman, J.L., 2009. Removal of phosphorus from solution using biogenic iron oxides. Water Res. 43, 2029–2035.
Rhoton, F.E., Bigham, J.M., Lindbo, D.L., 2002. Appl. Geochem. 17, 409–419.
Riedel, T., Zak, D., Biester, H., Dittmar, T., 2013. Iron traps terrestrially derived dissolved organic matter at redox interfaces. 110, 10101–10105.
Scarlett, N.V.Y., Madsen, I.C., 2006. Quantification of phases with partial or no known crystal structures. Powder Diffract. 21, 278–284.
Schwertmann, U., Cornell, R.M., 2000. WILEY-VCH Verlag GMBH & Co. KGaA, Weinheim, Germany.
Schwertmann, U., Stanjek, H., Becher, H.H., 2004. Long-term in vitro transformation of 2-line ferrihydrite to goethite/hematite at 4, 10, 15 and 25 degrees C. Clay Miner. 39 (4), 433–438.
Schwertmann, U., Wagner, F., Knicker, H., 2005. Ferrihydrite-humic associations: magnetic hyperfine interactions. Soil Sci. Soc. Am. J. 69, 1009–1015.
Sowers, T.D., Harrington, J.M., Polizzotto, M.L., Duckworth, O.W., 2017. Sorption of arsenic to biogenic iron (oxyhydr)oxides produced in circumneutral environments. Geochim. Cosmochim. Acta 198, 194–207.
Sowers, T.D., Holden, K.L., Coward, E.K., Sparks, D.L., 2019. Dissolved organic matter sorption and molecular fractionation by naturally occurring bacteriogenic iron (oxyhydr) oxides. Environ. Sci. Technol. 53, 4295–4304.
Stefánsson, A., Gíslason, S.R., 2001. Chemical weathering of basalts, Southwest Iceland: effect of rock crystallinity and secondary minerals on chemical fluxes to the ocean. Am. J. Sci. 301, 513–556.
Stefánsson, A., Gíslason, S.R., Arnórsson, S., 2001. Dissolution of primary minerals in natural waters - II.Mineral saturation state. 172, 251–276.
Stefánsson, A., Arnórsson, S., Sveinbjörnsdóttir, A.E., 2005. Redox reactions and potentials in natural waters at disequilibrium. Chem. Geol. 221, 289–311.
Swedlund, P.J., Miskelly, G.M., McQuillan, A.J., 2009. An attenuated total reflectance IR study of silicic acid adsorbed onto a ferric oxyhydroxide surface. Geochim. Cosmochim. Acta 73, 4199–4214.
Takahashi, Y., Châtellier, X., Hattori, K.H., Kato, K., Fortin, D., 2005. Adsorption of rare earth elements onto bacterial cell walls and its implication for REE sorption onto natural microbial mats. Chem. Geol. 219, 53–67.
Tessier, A., Fortin, D., Belzile, N., DeVitre, R.R., Leppard, G.G., 1996. Metal sorption to diagenetic iron and manganese oxyhydroxides and associated organic matter: narrowing the gap between field and laboratory measurements. Geochim. Cosmochim. Acta 60, 387–404.
ThomasArrigo, L.K., Mikutta, C., Byrne, J., Barmettler, K., Kappler, A., Kretzschmar, R., 2014. Iron and arsenic speciation and distribution in organic flocs from streambeds of an arsenic-enriched peatland. Environ. Sci. Technol. 48, 13218–13228.
ThomasArrigo, L.K., Byrne, J., Kappler, A., Kretzschmar, R., 2018. Environ.Sci. Technol. 52, 12316–12326.
ThomasArrigo, L.K., Kaegi, R., Kretzschmar, R., 2019. Ferrihydrite growth and transformation in the presence of ferrous Fe and model organic ligands. Environ. Sci. Technol. 53, 13636–13647.
Thompson, A., Rancourt, D.G., Chadwick, O.A., Chorover, J., 2011. Iron solid-phase differentiation along a redox gradient in basaltic soils. Geochim. Cosmochim. Acta 75, 119–133.
Vandenberg, E., De Grave, E., 2013. Application of Mössbauer spectroscopy in earth sciences. In: Yoshida, Y., Langouche, G. (Eds.), Mössbauer Spectroscopy. Springer, Berlin, pp. 91–185.
Vollrath, S., Behrends, T., Koch, C.B., Van Cappellen, P., 2013. Effects of temperature on rates and mineral products of microbial Fe(II) oxidation by Leptothrix cholodnii at microaerobic conditions. Geochim. Cosmochim. Acta 108, 107–124.
Wartchow, R., 1997. Crystal structure of potassium tris(oxalato)ferrate(III) trihydrate doped with sodium, K2.9Na0.1Fe(C2O4)3.3H2O. Z. Krist.-New. Cryst. St. 212, 83–84.
Waychunas, G.A., Rea, B.A., Fuller, C.C., Davis, J.A., 1993. Surface chemistry of ferrihydrite: part 1. EXAFS studies of the geometry of coprecipitated and adsorbed arsenate. Geochim. Cosmochim. Acta 57, 2251–2269.
Whitaker, A.H., Duckworth, O.W., 2018. Cu, Pb, and Zn sorption to biogenic iron (oxyhydr)oxides formed in circumneutral environments. Soil Syst. 2, 1–21.
Whitaker, A.H., Peña, J., Amor, M., Duckworth, O.W., 2018. Cr(VI) uptake and reduction by biogenic iron (oxyhydr)oxides. 20, 1056–1068.
Zabinsky, S.I., Rehr, J.J., Ankudinov, A., Albers, R.C., Eller, M.J., 1995. Multiple-scattering calculations of X-ray absorption spectra. Phys. Rev. B 52, 2995–3009.
Zhao, Q., Dunham-Cheatham, S., Adhikari, D., Chen, C.M., Patel, A., Poulson, S.R., Obrist, D., Verburg, P.S.J., Wang, X.L., Roden, E.R., Thompson, A., Yang, Y., 2020. Oxidation of soil organic carbon during an anoxic-oxic transition. Geoderma 377, 114584.
Zhukhlistov, A.P., 2001. Crystal structure of lepidocrocite FeO(OH) from the electron-diffractometry data. Crystallogr. Rep. 46, 730–733.